Opportunistic Time Synchronization Using Signals From Low Earth Orbit Communications Satellites

by

Landon Boyd

A thesis submitted to the Graduate Faculty of
Auburn University
in partial fulfillment of the
requirements for the Degree of
Master of Science

Auburn, Alabama
December 14, 2024

Keywords: Signal of Opportunity, Precise Timing, Navigation, LEO

Approved by

David M. Bevly, Chair, Bill and Lana McNair Professor of Mechanical Engineering
Scott Martin, Assistant Research Professor of Mechanical Engineering
Dan Marghitu, Professor of Mechanical Engineering

Abstract

This thesis develops a receiver that is capable of utilizing opportunistic pseudorange, Doppler shift, and Angle of Arrival (AoA) measurements to jointly estimate precise receiver time as well as satellite position states. To accomplish this, the multi-antenna receiver is placed at a known, stationary location, with distances between antennas fully determined beforehand. The aforementioned measurements are inputs to an Iterated Extended Kalman Filter (IEKF) algorithm, the outputs of which are estimates of the receivers clock offset and clock drift.

Precise timing is a foundational technology that enables the modern world we live in. Currently, the Global Positioning System (GPS) and other Global Navigation Satellite Systems (GNSS) provide the backbone for precise timing infrastructure. As GPS dependence grows, so does technological vulnerability when it is unavailable. This thesis focuses on using signals from Low Earth Orbit (LEO) communications satellites to act as a precise timing holdover technology in the absence of GPS.

To validate the design, a series of Monte Carlo (MC) studies were performed using a high fidelity simulation environment. A LEO SOP noise profile, along with simulated LEO satellites allowed for receiver analysis with varying baseline lengths and clock oscillator qualities. The receiver was found to be able to determine clock error relative to the LEO network to an accuracy of under 1 μs.

Acknowledgments

I'd like to thank my wife Brooke for supporting and encouraging me always. I'd also like to thank my parents for raising and educating me, as well as my brothers for keeping life interesting.

Table of Contents

List of Figures

List of Tables

Chapter 1

Introduction

1.1 Background and Motivation

The advent of Global Navigation Satellite Systems (GNSS) for reliable position, navigation, and timing (PNT) has led to an explosion of new technologies that are now indispensable. GNSSs like the Global Positioning System (GPS), Galileo, and Glonass provide essential information to emergency workers, military personnel, the scientific community, and industry partners worldwide. Access to consistent and accurate positioning and timing information has led to consumer innovations as well, enabling much of the convenience we expect in our daily lives.

While most people associate GPS with position location, the satellites also serve an equally important lesser-known purpose. GPS is responsible for disseminating precise timing to devices across the globe. This process is called time transfer and is an enabling technology for many modern necessities we take for granted. For this reason, GPS is crucial to government, industry, and civilian user alike [1]. GPS provides time synchronization to Coordinated Universal Time (UTC) with errors as low as 30 nanoseconds [2]. Attaining these precise timing solutions relies on the process of acquiring, tracking, and decoding signals sent from GPS satellites in Medium Earth Orbit (MEO). However, the huge distance to these satellites, earth atmospheric conditions, and obstructions like buildings or foliage all reduce the strength of the signal. This reduced strength leaves GNSS signals vulnerable, which in turn leaves all applications that rely on them vulnerable.

In addition to these natural threats, GPS jamming and spoofing devices are becoming cheaper and easier to operate [3, 4]. GPS jammers broadcast noise in the same radio frequency band as GPS, disrupting the acquisition and tracking process. Simple handheld GPS jammers are capable of disrupting access to precise GPS timing over large areas without warning, leaving many critical applications at risk. GPS spoofing occurs when a malicious actor broadcasts fake GPS signals designed to mislead GPS users. These spoofing attacks have the capability to introduce large timing errors wherever a GPS receiver is used. These threats pose a difficult challenge, and the stakes are high due to the large number of users relying on constant GPS positioning and timing.

Because of these reliability concerns, this thesis develops a technique for maintaining stringent timing requirements apart from the use of GNSS. To accomplish this, signals being broadcast from low earth orbit (LEO) satellites are exploited to aid a receiver in estimating its time error. LEO satellites are usually not intended for this purpose, and thus they are referred to as signals of opportunity (SOP). LEO SOPs carry a key advantage in that their received signal power can be up to 1000 times stronger than their GNSS counterparts in MEO [5]. This incredible signal strength has the potential to mitigate concerns over the vulnerability of GNSS.

To maintain timing accuracy with LEO SOPs, a multi-antenna receiver is utilized to estimate user clock states and LEO emitter position and velocity states. This receiver works by using code phase and carrier phase received from LEO communications satellites to obtain the direction and distance to available emitters. These measurements are incorporated into a filter to estimate the clock bias and drift of a receiver at a known location in a process called time transfer. To validate receiver design, a simulation study is carried out to assess performance in a series of Monte Carlo (MC) simulations.

1.2 Prior Art

The concept of using LEO satellite emitters as an augmentation to vulnerable GNSS has been the focus of much recent work. The next three subsections describe the current research effort towards using LEO satellites for robust timing.

1.2.1 Standalone LEO PNT

Opportunistic positioning using ranges from LEO satellites is considered in [6, 7]. These methods utilize completely opportunistic signal tracking, obtaining position results from communication satellites in LEO orbit for which the user doesn't own a subscription. Whenever ranging methods are considered, timing accuracy is directly tied to user positioning accuracy and transmitting clock accuracy. In the case of opportunistic measurements, the transmitting clocks are generally not designed for phase stability commensurate with GNSS ranging accuracy [8]. To overcome this limitation, research into refining LEO clock states is ongoing.

Kunzi and Montenbruck demonstrated that a LEO satellite's oscillator could be disciplined to GNSS oscillators to nanosecond-level accuracy [9]. In [9], a LEO satellite's low quality oscillator was refined using an onboard GNSS receiver to maintain a high timing accuracy that was sufficient to provide opportunistic range measurements. Since LEO satellites have constant, direct line of sight to MEO navigation satellites and are much closer to the signals than a receiver on earth, they do not have the same vulnerability concerns as receivers on the ground.

While synchronizing LEO satellites to GNSS and performing opportunistic ranging is a promising research thrust for timing synchronization, it still has drawbacks. To perform time transfer with ranging, satellite positions must be known beforehand. This is not a problem for GPS, as its position is broadcast in the ephemeris message that receivers can receive and interpret. For LEO that don't broadcast such a message, publicly available satellite information must be used. This information comes in the form of two line element (TLE) files, and usually carry gross inaccuracies [10]. These errors inherently limit time transfer accuracy, making this method also not suitable to meet modern timing needs.

Another way to overcome limited LEO timing accuracy is by using differential methods [11, 12]. These techniques involved taking the difference of measurements collected at a known base station and an unknown rover. With this difference, the rover can localize itself relative to the known base station. While this process has been shown to yield good positioning results,

it cannot provide time synchronization. The process of differencing only allows for knowledge of relative clock errors between the user and rover, leaving the user unable to synchronize time.

In recent years, companies have started to take on the challenges of LEO PNT [13, 14]. These technologies promise centimeter-level positioning independently of GPS, promising redundancy to critical systems. However, the satellites and navigation signals are currently only technology demonstrators and cannot yet provide PNT services. While these satellites will almost certainly bolster PNT infrastructure in the future, those gains have yet to be realized.

1.2.2 Augmentation LEO PNT Constellations

The most precise time transfer currently available from satellites is obtained via Precise Point Positioning (PPP). PPP is performed by resolving carrier phase ambiguities present in GNSS measurements, and eliminating these ambiguities to obtain high-accuracy range measurements [15, 16, 17]. This effectively means that a PPP receiver knows its location to the centimeter level, and time to the sub-nanosecond level.

Augmenting GNSS PPP techniques with LEO satellites has shown better convergence times than with GNSS alone [18, 19]. This shows that LEO constellations promise to contribute to the field of timing research in the future, as the simulated constellations in these papers eventually become reality. These studies, however, used LEO only to augment GNSS and did not consider them as an entirely different backup source. This overlooks the inherent vulnerability of GNSS, therefore not fully addressing the problem. Additionally, as was stated in the previous section, purpose-built LEO PNT satellites are still in development.

1.2.3 The Iridium STL Signal

Currently, the Iridium Satellite Time and Location (STL) signal is the only LEO standalone timing solution [20, 21]. Leveraging an already existing global satellite communications network, Iridium satellites now offer the specialized STL signal that is designed for ranging and time synchronization. Tests of Iridium STL are very promising, and have been shown to consistently yield sub-microsecond accuracy, even indoors [22]. Additionally, Iridium's global

Figure 1.1: Iridium NEXT Satellite

reach mean that STL can deliver precise time anywhere on Earth. The Iridium NEXT satellite platform that offers STL is shown in Figure 1.1.

Compared to opportunistic methods, however, STL carries drawbacks. Because STL is only deployed on a single satellite constellation, the Iridium satellite network, it cannot realize two critical benefits of opportunistic navigation: signal diversity and favorable satellite geometry. These properties will be discussed in the coming chapters. The STL network alone can provide neither good satellite geometry nor signal diversity, making it susceptible to the same failure modes of GPS.

1.3 Contributions and Outline

This thesis develops a novel method to provide timing synchronization to a receiver of known location using LEO satellites as SOPs. Recent research has focused on building LEO PNT constellations or augmenting existing constellations, but both of these thrusts fail to realize the benefits of SOPs. In order to use these unique signals to our advantage and provide precise time, this thesis presents the following contributions:

- Implementation of a standalone precise timing solution that can operate independently of GPS
- Design of a noise model for LEO satellite emitters based on real LEO satellite data

- Analysis of the timing solution in a series of Monte Carlo simulations to predict real world system error
- Publication and presentation of receiver results in the ION Pacific PNT Conference in April 2022 [23]

1.4 Thesis Outline

This thesis will describe the development of the proposed receiver and the simulation study designed to validate its performance. Chapter 2 will more fully describe why a standalone timing solution is necessary and will also discuss some inherent limitations in SOPs. Chapter 3 will outline how the proposed receiver will overcome the limitations of these SOPs to perform time synchronization. It will also describe LEO constellations and the time scale that the proposed receiver will use for synchronization, as well as the estimator used, the Iterated Extended Kalman Filter. Chapter 4 describes an experimental study whose aim is to develop a noise model for LEO ranging. This noise model is necessary to ensure that the results of this thesis align with real world expectations of performance. Chapter 5 describes the Monte Carlo simulation studies aimed at determining performance benchmarks for the receiver in a variety of scenarios. Results of these Monte Carlo simulations will be shown, verifying that the receiver can act as a standalone timing solution. Finally, Chapter 6 gives final conclusions as well as proposed future work.

Chapter 2

Precise Timing Background

2.1 Overview of Time Transfer

This section introduces the basic technologies related to time scales and time transfer. These technologies are introduced as critical enablers for the world we live in. Time transfer allows for synchronization across the globe, enabling communications, trade, scientific applications, and more.

2.1.1 History of Time Transfer Technologies

The era of modern, standardized time began in 1855 when Britain established the first common time scale, Greenwich Time. Prior to common time scales, people set their clocks to local timescales, causing inefficiency as railways and passenger transit led to greater interconnection. With the advent of Greenwich Time, users across Britain knew when to expect railways and public broadcasts, increasing efficiency. In the 1960's, the global community agreed on a standardized time scale for the entire world, Coordinated Universal Time (UTC). UTC brought the benefits of synchronization to the entire globe, fostering greater connection which led to trade and communication advantages.

While it is universally agreed that synchronizing all users to a common time scale is advantageous, the process of performing this synchronization is less than trivial and is known as time transfer. Greenwich Time transfer was performed over telegram, offering acceptable accuracy at the time [24]. Indeed, telegram and telephone were the standards for time transfer well into the 20th century, when the need emerged for more accurate synchronization techniques.

With time transfer, users with low quality clocks can synchronize their timepieces to high quality clocks. Due to cost, size, and power constraints, equipping every watch or mobile phone user with a high quality atomic clock is infeasible. Cheaper, low accuracy temperature-compensated crystal oscillators (TCXO) are ideal for such applications. Time transfer is used to constrain the error growth on these low quality clocks by disciplining them to a high accuracy master clock, thereby empowering consumer devices with extremely accurate timing information. This capability is extremely advantageous to a variety of industrial sectors.

For example, cell phone communications are completely dependent on precise time to function. 5G cellular uses an encoding called Orthogonal Frequency Division Multiple Access (OFDM). OFDM allows multiple users to transmit and receive simultaneously on different subcarrier bands, requiring precise synchronization to prevent drifting into another user's band [25]. Without precise time available at the cell phone tower, user's transmissions would overlap, causing disruption of service.

Precise time transfer is also used to increase the performance of the power grid. Using microsecond accurate time, utility providers identify faults and balance power distribution across the grid [26]. This technology enables utilities providers to stretch the capabilities of the power grid, but real time monitoring is impossible without precise time. Without it, users would likely overload the already strained system, leading to outages that could result in harm and chaos.

For these and most other modern applications, GPS has become the gold standard of time transfer technology. The newest GPS satellites contain 3 Rubidium atomic clocks, each of which are steered to an even higher quality ensemble of atomic clocks [27, 28]. GPS has become the standard for time transfer because of its precise timescale and freely available timing measurements, both of which will be described in the next sections. Were this technology to become unavailable or obstructed in any way, the results could be severe.

2.1.2 GPS Time

The internationally recognized timescale is UTC, maintained by The Bureau International des Poids et Mesures (BIPM) in France [29]. UTC is calculated by taking measurements from high quality atomic clocks all around the world, and combining them in a weighted average [30].

Strictly speaking, UTC is not physically obtainable in real time, as it requires international laboratories like the National Institute of Standards and Technology (NIST) and the United States Naval Observatory (USNO) to share timing data that allows true UTC to be estimated. To overcome this limitation, precise time from each of these laboratories is disseminated to users many days before UTC is calculated. For instance, if a user were synchronizing to the master clock at NIST, they are said to be synchronized with UTC(NIST) [31]. There are more than 80 such timing standards across more than 60 nations that a user can synchronize to. The Global Positioning System utilizes UTC as distributed by the USNO, UTC(USNO). More specifically, a timescale called GPS Time (GPST) is maintained based off UTC(USNO).

The high quality ensemble of atomic clocks at the Naval Observatory in Washington, D.C. ensure that GPS Time is accurate to true UTC to within 30 nanoseconds [2]. To accomplish this, the USNO maintains an ensemble of over 100 extremely accurate atomic clocks that steer UTC(USNO). Additionally, should anything happen to the Naval Observatory, an alternate master clock for the GPS satellites is operated out of Schriever Space Force Base in Colorado [32]. Schriever Space Force Base is also the master control station for all GPS satellites, making it their responsibility to ensure that all GPS satellites are synchronized to GPS Time.

The clocks on board the GPS satellites drift from GPST due to inaccuracies in their on-board frequency standards. The ground control segment of the GPS constellation must monitor these errors and issue corrections for them. To do this, ground stations all over the world collect measurements from overhead GPS satellites and transmit this information to the GPS Master Control Station. Here, individual satellite clock phase deviation from GPS Time is estimated and predicted into the future using a quadratic polynomial fit [33]. The coefficients of this polynomial are broadcast by the GPS satellites in the navigation message so that users can apply them in order to synchronize each satellite's clock to GPST.

GPS Time enables all of the fundamental services that GPS users expect and depend on. Maintaining this timescale and synchronizing all of the satellites to it requires ground monitoring stations across the globe, dozens of highly accurate atomic clocks, and sophisticated filtering algorithms to blend their measurements while maintaining strict adherence to the international timescale, UTC. With the foundation for this remarkable technology laid, the next

two sections detail how a user equipped with a GPS receiver can synchronize their local clocks to GPS time in a process known as time transfer.

2.1.3 Standard GPS Time and Frequency Transfer

With an accurate timescale and over 30 orbiting clocks accurately synchronized to it, the last step in time transfer is left to the end user. Time transfer occurs when a GPS receiver calculates its offset and drift from GPS Time and corrects its onboard clock accordingly. To enable this, GPS satellites broadcast signals on three different link frequencies, shown in Table 2.1.

Table 2.1: GPS Link Frequencies [34]

Band	L_1	L_2	L_5
Frequency (MHz)	1575.42	1227.6	1176

For a GPS receiver, positioning and time transfer occur simultaneously when a sufficient number of satellites are in view and their signals tracked. Since the process of tracking the GPS signals being broadcast on the three link frequencies is beyond the scope of this work, the curious reader is referred instead to [34, 35]. The process of tracking produces three primary observables used in time transfer: code phase, carrier phase, and carrier frequency.

GPS code phase measurements are used to generate pseudorange measurements. Pseudoranges are measured by multiplying the speed of light by the time of flight of the GPS signal, as is shown in Equation (2.1). The time of flight is the difference between the reception time t_R and the transmission time t_t.

$$\tilde{\rho}^k = c(t_R - t_t) \tag{2.1}$$

To actually get a pseudorange, the receiver must track the signal to obtain the GPS Time of Week (TOW) in seconds, which is a counter in seconds that rolls over between Saturday and Sunday night each calendar week. The receiver then guesses the signal reception time, and calculates a pseudorange using the propagation speed of the signal (light speed). For estimation purposes, the pseudorange is modeled as a combination of the range between the satellite and the receiver as well as a collection of bias terms that arise from the propagation channel. This

pseudorange model is shown in Equation (2.2).

$$\hat{\rho}^k = \sqrt{(x^k - x_u)^2 + (y^k - y_u)^2 + (z^k - z_u)^2} + c(\delta t_u - \delta t^k) + I + T + M + \epsilon \tag{2.2}$$

In this equation, $\tilde{\rho}^k$ is the pseudorange measurement from satellite k. The first term on the left-hand side of the equation under the radical represents the true geometric range from satellite k to the user, denoted u. The second term is the speed of light, c multiplied by the combined errors of the user clock, δt_u, and satellite k's clock, δt^k. I represents the error introduced by the ionosphere, and T from the troposphere. M is error introduced by multipath effects, and ϵ is white noise introduced by the channel and receiver. In Equation (2.2), δt_u is referred to as user clock bias, and must be estimated so the user can align their time with GPS time.

To solve for this bias, at least four GPS satellites must be in view. This allows the user to solve for the four unknowns in each pseudorange equation, $x_u, y_u, z_u, \delta t_u$. T and M are neglected for this basic analysis due to their relatively small impact on the solution during nominal operating conditions. I can be solved for using dual frequency GPS, and is also neglected [34]. The simplified pseudorange equation is shown in Equation (2.3).

$$\tilde{\rho}^k = \sqrt{(x^k - x_u)^2 + (y^k - y_u)^2 + (z^k - z_u)^2} + c(\delta t_u - \delta t^k) + \epsilon \tag{2.3}$$

As was discussed in Section 2.1.2, GPS satellites' clocks are constantly monitored by GPS ground control, meaning that the satellite clock error δt^k in Equation (2.3) is known. This offset is broadcast in the GPS message so GPS receivers can eliminate it from range measurements. Since the range equation is nonlinear, Newton-Rahpson recursive least squares is used to estimate the states of interest. The nonlinear optimization problem can be expressed as shown in Equation (2.4).

$$\mathbf{y} = h(\mathbf{x}) \tag{2.4}$$

In the generic nonlinear problem shown in Equation (2.4), $\mathbf{y}$ is a $1xm$ vector of range measurements, and $h(\mathbf{x})$ is the nonlinear function of the four states.

$$\mathbf{y} = \begin{bmatrix} \tilde{\rho}^1 \\ \tilde{\rho}^2 \\ \vdots \\ \tilde{\rho}^m \end{bmatrix} \tag{2.5}$$

$$\mathbf{x} = \begin{bmatrix} \hat{x}_u \\ \hat{y}_u \\ \hat{z}_u \\ \hat{\delta t}_u \end{bmatrix} \tag{2.6}$$

The solution to the equations in $\mathbf{y}$ is iterative in nature. The GPS receiver makes an initial guess of the solution, $\hat{\mathbf{x}}$. The pseudorange equations are then linearized about this state vector using a Taylor series expansion. The constant and first order terms are kept to ensure the resulting approximation is linear. After expansion and collection the linearized pseudorange model appears in the form shown in Equation (2.7).

$$\tilde{\rho}^k \approx \rho^k|_{x=\hat{x}_0} - u_{uk,x}(x_u - \hat{x}_u) - u_{uk,y}(y_u - \hat{y}_u) - u_{uk,z}(z_u - \hat{z}_u) + c(\delta t_u - \hat{\delta t}_u) \tag{2.7}$$

In the above equation, u_{uk} refers to the unit vector pointing from the user estimate to the known satellite location. x_u, y_u, z_u and δt_u refer to the true values for ECEF X, Y, Z and user clock bias. After collecting m pseudorange measurements, the problem can be expressed linearly as shown in Equation (2.8).

$$\begin{bmatrix} \tilde{\rho}^1 - \hat{\rho}^1 \\ \tilde{\rho}^2 - \hat{\rho}^2 \\ \vdots \\ \tilde{\rho}^m - \hat{\rho}^m \end{bmatrix} = \begin{bmatrix} -u_{u1,x} & -u_{u1,y} & -u_{u1,z} & 1 \\ -u_{u2,x} & -u_{u2,y} & -u_{u2,z} & 1 \\ \vdots & \vdots & \vdots & \vdots \\ -u_{um,x} & -u_{um,y} & -u_{um,z} & 1 \end{bmatrix} \begin{bmatrix} x_u - \hat{x}_u \\ y_u - \hat{y}_u \\ z_u - \hat{z}_u \\ \delta t_u - \hat{\delta t}_u \end{bmatrix} \tag{2.8}$$

Equation (2.8) is further simplified to Equation (2.9).

$$\delta \mathbf{y} = H \delta \mathbf{x} \tag{2.9}$$

The above system of equations is solved iteratively. $\delta \mathbf{x}$ is called the state correction, and is calculated by the Least Squares method in Equation (2.10).

$$\delta \mathbf{x} = (H^T H)^{-1} H^T \delta \mathbf{y} \tag{2.10}$$

The correction is applied by to the state in Equation (2.11)

$$\hat{\mathbf{x}} = \hat{\mathbf{x}} + \delta \mathbf{x} \tag{2.11}$$

The correct and update cycle in Equations (2.10-2.11) continues until the correction, $\delta \mathbf{x}$ becomes sufficiently small. At this point, the solution is said to have converged. The user is able to subtract the estimated clock bias from their current time such that they are synchronized to GPS Time.

Frequency transfer follows a very similar process to time transfer. For frequency transfer, carrier frequency is used along with knowledge of the link frequencies in Table 2.1 to calculate the Doppler shift between the satellite and the user. This Doppler shift is equal to the pseudorange rate scaled by the wavelength of the signal, λ [34]. The pseudorange rate measurement provided by the Doppler shift calculation is modeled according to Equation (2.12).

$$\dot{\rho}^k = \dot{r}^k + (\dot{\delta t}_u + \dot{\delta t}^k) + \epsilon_{\dot{\phi}}^k \tag{2.12}$$

The above equation resembles the pseudorange equation (Equation (2.3)), except it relates the measurement to the velocity and drift states of the system instead of the position and bias states. The satellite clock bias, $\dot{\delta t}^k$ is provided in the ephemeris message, producing negligible error. The range rate $\dot{r}^k$ can be obtained by differentiating the geometric range term of Equation (2.3),

and is shown in Equation (2.13).

$$\dot{r}^k = \left(\mathbf{v}^k - \mathbf{v}_u\right) \cdot \mathbf{u}_{uk} \tag{2.13}$$

In this expression, the satellite velocity vector $\mathbf{v}^k$ is known because of the same ephemeris calculations that yielded satellite position. The unit vector from user to satellite $\mathbf{u}_{uk}$ is the same unit vector that was used to solve Equation (2.8), meaning that estimating clock drift must occur jointly with bias estimation. Substituting Equation (2.13) into (2.12) and moving all known terms to the right side yields Equation (2.14).

$$\dot{\rho}^k - \left(\mathbf{v}^k \cdot \mathbf{u}_{uk}\right) = -\mathbf{u}_{uk} \cdot \mathbf{v}_u + \dot{\delta t}_u + \epsilon_{\dot{\phi}}^k \tag{2.14}$$

Similarly to position and bias estimation, these Doppler shift measurements can be stacked into a vector and the user velocity and drift states can be solved with least squares. Unlike position and bias estimation, however, the resulting set of equations is linear, and can be solved without any recursion. The resulting problem is shown in Equation (2.15).

$$\begin{bmatrix} \dot{\rho}^1 - (\mathbf{v}^1 \cdot \mathbf{u}_{uk}) \\ \dot{\rho}^2 - (\mathbf{v}^2 \cdot \mathbf{u}_{uk}) \\ \vdots \\ \dot{\rho}^m - (\mathbf{v}^m \cdot \mathbf{u}_{uk}) \end{bmatrix} = \begin{bmatrix} -u_{u1,x} & -u_{u1,y} & -u_{u1,z} & 1 \\ -u_{u2,x} & -u_{u2,y} & -u_{u2,z} & 1 \\ \vdots & \vdots & \vdots & \vdots \\ -u_{um,x} & -u_{um,y} & -u_{um,z} & 1 \end{bmatrix} \begin{bmatrix} \hat{\dot{x}}_u \\ \hat{\dot{y}}_u \\ \hat{\dot{z}}_u \\ \hat{\dot{\delta t}}_u \end{bmatrix} \tag{2.15}$$

The user states can be solved with Least Squares directly, yielding a user velocity vector and a user clock drift estimate in Equation (2.16).

$$\hat{\mathbf{x}} = (H^T H)^{-1} H^T \mathbf{y} \tag{2.16}$$

The estimated clock drift represents the frequency difference between the receiver's onboard oscillator and the oscillator driving GPST. This frequency difference can then be wiped off from future measurements. Figure 2.1 shows results from estimating the clock bias and drift for a Novatel GPS receiver. Without estimation, receiver clock bias would be nearly millisecond

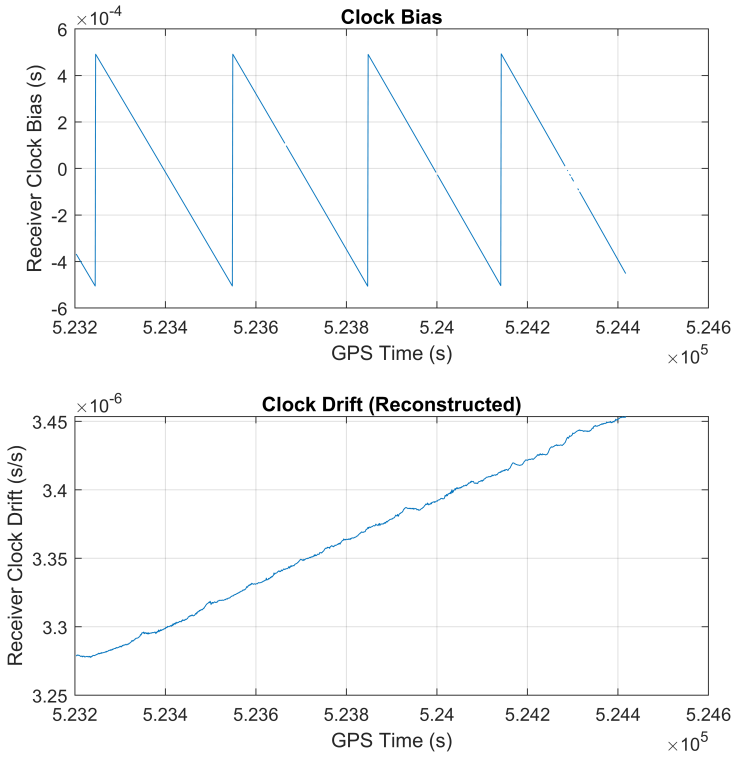

Figure 2.1: Clock Bias and Drift Estimation on a Novatel GPS Receiver

level, which is too imprecise for most timing-based applications. This example highlights the necessity of GPS time transfer in everyday life.

2.1.4 Precise GPS Time Transfer

For most applications, the time transfer accuracy afforded via joint position and time estimation is sufficient. This is because this method is satisfactory to within 1 μs, which is the benchmark for most industrial applications [36]. When time is needed down to single nanosecond level or better, the user must utilize carrier phase-based techniques.

If the GPS receiver maintains constant tracking of a GPS satellite, then the carrier phase of the received signal can be treated as a high quality range. To see why this is the case, the received signal model for GPS carrier phase is shown in Equation (2.17), taken from [34].

$$\phi^k = -\frac{1}{\lambda}[r + I_\phi + T_\phi] + \frac{c}{\lambda}(\delta t_u - \delta t^k) + N^k + \epsilon_\phi \tag{2.17}$$

In this equation, ϕ^k is the accumulated carrier phase from satellite k since tracking began assuming no interruptions in tracking. The true geometric range is represented by r, and I_ϕ and

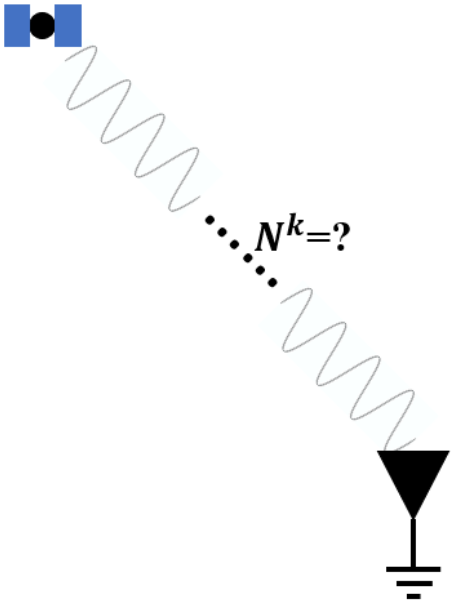

Figure 2.2: Illustration of Integer Ambiguity

T_ϕ are specially denoted to distinguish them from their pseudorange counterparts in Equation (2.2). λ is the wavelength of the sinusoidal carrier, in meters. N^k is an integer bias representing the true number of carrier phase cycles between the user and the emitter. Finally, ϵ_ϕ is the noise, distinguished again from the noise in Equation (2.2).

This carrier phase measurement is extremely precise compared to the pseudorange measurement because the Phase Locked Loops (PLLs) that determine carrier phase can be accurate to within 1%-2% of the carrier's wavelength, λ. For the standard GPS L1 signal frequency taken from Table 2.1, λ is around 19 centimeters, meaning PLL error can be on the order of millimeters. These levels of accuracy can be on the single nanosecond level, or in some cases on the scale of hundreds of picoseconds [15]. As was mentioned in the previous chapter, positioning with these ultra-precise measurements is called Precise Point Positioning.

The primary challenge of PPP is to determine the value of the integer bias (N) in Equation (2.17), which is referred to as the carrier phase ambiguity. Solving these ambiguities usually takes much longer than forming a basic GPS solution, as estimators need more convergence time and successive measurements to narrow down the integer search space [17]. An illustration of this concept is given in Figure 2.2.

This process of solving for the integer bias is quicker and produces more accurate results if the user location is known, which for many timing applications is the case [15, 37]. Examples of known locations that utilize time transfer include cell phone towers, power plants, and data centers.

2.2 GPS Vulnerabilities

This section describes the many threats facing users of GPS time transfer. Because GPS provides free to use and globally available signals, it has become the de facto solution for precise timing. This ubiquity has been a technological enabler for many of the convenient services we use today. However as reliance on GPS has grown steadily, so has its potential to be a singular point of failure for many critical applications. This is dangerous, since GPS is susceptible to a variety of faults and failure modes. These modes are primarily due to GPS' extremely low received signal power, which for a civilian user is approximately 10^{-16} watts [34]. GPS receivers use a combination of techniques to boost the power of the received signal and extract the necessary information for position and time estimation. However, the low signal power means that a variety of different conditions can work to make GPS unavailable. These conditions are described in the following subsections.

2.2.1 Urban Environments

Urban environments have proven to be especially challenging operating conditions for standard GPS receivers [38]. Since GPS signals are very weak, buildings and vehicles can easily obstruct them, stressing the tracking and estimation algorithms required for GPS to function. Even worse, urban canyons can also reflect GPS signals in a process known as multipath. Multipath signals confuse GPS receivers, as the 'echos' it produces can obfuscate the true signal. Figure 2.3 illustrates these two challenges.

Urban centers contain most of the infrastructure elements that require precise timing capabilities like cell towers and power plants. Unfortunately, these environments can also cause these services to be the most vulnerable, as an unfavorable RF environment can cause degraded GPS solutions.

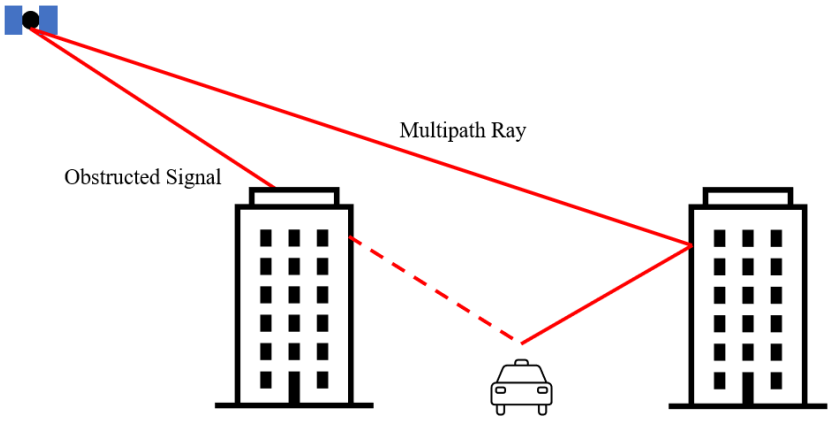

Figure 2.3: GPS Errors in Urban Environments

2.2.2 Radio Frequency Interference

GNSS are extremely vulnerable to radio frequency (RF) interference. Because of the low power of GPS signals, interference on the order of milliwatts can disrupt service, causing a host of issues. A 2 watt jammer tested by the British government disrupted GPS across a 30 kilometer stretch of the North Sea, and similar models are available online [3]. A device unintentionally emitting on the L_1 band caused a GPS outage for a 50 nautical mile radius around the Denver International Airport in 2022 [39]. Perhaps even more concerning are the GPS outages where a cause is never pinpointed, as was the case at Dallas-Fort Worth International Airport in October 2022 [40]. Illegal GPS jamming devices are easily obtainable, cheap to operate, and very dangerous.

The scope of this problem can be seen on the GPS jamming map in Figure 2.4, obtained from [41]. The map shows the probability of GPS interference across the Middle East and part of the Balkans on July 3, 2024. Convenient access to GPS jamming has changed the landscape of modern warfare, and hospitals, cell towers, and internet providers miles away from physical danger can still find themselves without essential GPS services. This leads to inconvenience, financial loss, and potentially danger to a large number of people.

Another RFI scenario that can damage time transfer capabilities is spoofing. A spoofing attack occurs when false GPS signals are broadcast to confuse and mislead GPS users [4, 42]. Spoofing attacks have demonstrated themselves very effective, and can be carried out with

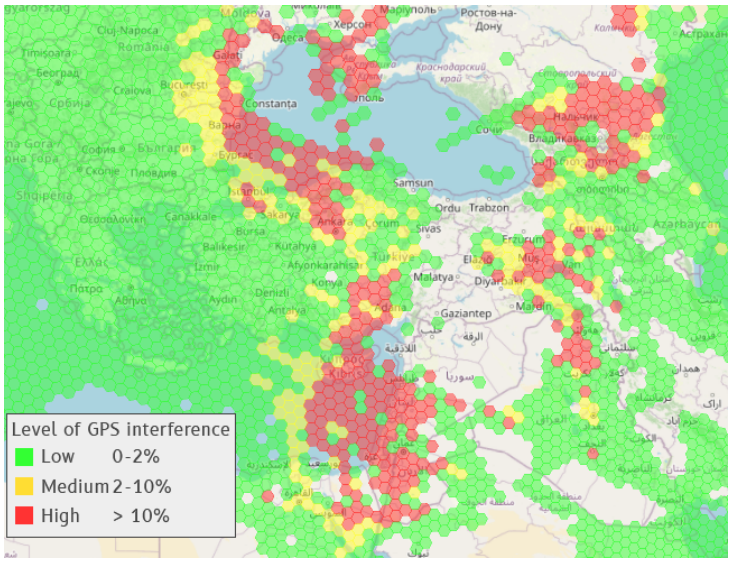

Figure 2.4: GPS Jamming Map of the Balkans and Middle East, July 3, 2024 [41]

modest hardware. As technology advances, more and more malicious actors will be taking advantage of readily available GPS jamming and spoofing technologies. Critical systems that rely on precise time need to be readied so that essential services can be maintained without interruption.

2.2.3 Natural Effects

All of the RF interference mentioned thus far has been man made, whether intentional or unintentional. However, many natural effects can weaken or even disrupt GNSS without malicious actors present. One such source of obstruction is foliage, which has been shown to cause tens of meters of ranging error in certain conditions [43]. Foliage can cause signal diffraction, obstruction, and multipath.

Additionally, solar flares and space weather can cause signal disruptions affecting GPS users. These events cause high total electron count in the ionosphere and momentary disruptions in PLL tracking known as cycle slips. Geomagnetic storm positioning error can be hundreds of meters [44]. Even in non extreme events, scintillation of the ionosphere can cause drastic changes in GPS position and timing solutions [45].

2.3 Signals of Opportunity (SOP)

This section describes the current state of research into augmentation and backup technologies that could be used to bolster and protect GPS position and time in the event of an outage. One such backup strategy is to use SOPs. A SOP is a signal that was not engineered with navigation or timing in mind, but can be non-cooperatively exploited for such purposes. In particular, signals from LEO communications satellites show great promise as SOPs. Since LEO satellites occupy a much lower altitude orbital band than GNSS, they do not suffer from the same failure modes as GPS. Their close proximity to the Earth's surface gives them high received power, cutting through jamming and foliage obstruction. Increased satellite density and quickly changing geometry can alleviate poor visibility in urban scenarios. For these reasons, LEO SOPs are the focus of this thesis.

2.3.1 Unknown Emitter Locations

To use traditional ranging methods for clock synchronization, the location of the satellite emitter must be known beforehand. In GPS and other GNSS, this is not an issue as a set of broadcast ephemeris can be obtained during the tracking stage. This broadcast ephemeris is used to calculate a GPS satellite location that is highly accurate, with under 10 meters of error [34]. This is accomplished through an extensive, worldwide monitoring network that can precisely determine each GPS satellite's orbit. These precise orbits are incorporated into the broadcast ephemeris message, producing the high quality position and timing estimates that GPS users rely upon. LEO SOPs, on the other hand, do not have this level of ground support. Since the emitters are broadband satellites that deliver internet and other communications services, their locations do not have to be known precisely. This means no precise satellite ephemeris or position data is available to the opportunistic user.

The best opportunistically available LEO satellite position information comes from the North American Aerospace Defense Command [46]. These published locations are in two-line element (TLE) data files, and contain rough ephemeris information on all LEO satellites. These ephemerides are accurate to tens of kilometers, meaning any received range errors will

be similarly corrupted [10]. Since publicly available TLE data is so inaccurate, many opportunistic methods focus on refining TLE positions while positioning simultaneously [47, 48]. For any opportunistic user, emitter locations are one of the primary barriers to navigation. The LEO satellite positions must either be refined or estimated completely if they are to produce observables that are good enough for positioning or timing.

2.3.2 Emitter Clock States

On top of the inaccurate satellite position information, LEO satellites usually have much worse clocks than their GNSS counterparts. Most LEO emitters are intended as communications satellites, examples being Iridium, Starlink, and Orbcomm. Subscribers to the network don't range off the satellites they are linked to, which means that the satellites themselves can afford to have less accurate clocks. Whereas GPS satellites are equipped with high quality Rubidium atomic clocks, LEO satellites often come with oven-controlled crystal oscillators (OCXOs) or chip scale atomic clocks (CSACs). These lower cost alternatives provide poorer ranging accuracy, and must be accounted for when using LEOs as SOPs.

Perhaps worse than lower quality clocks is the fact that LEO satellites' clock states are unknown. While GPS clocks broadcast clock corrections generated by a ground control segment, LEO satellites' clocks are free to drift without affecting their intended purpose, i.e., communication. This means that using them to synchronize to UTC would be impossible without knowing or estimating their onboard clock errors.

LEO satellite operators don't maintain a master timescale like the United States Navy, and often LEO satellites operate with onboard GPS receivers for time synchronization [49]. LEO satellites have special GPS receivers built to operate in space, and use time transfer to constrain the drift of their own clocks. While this implies that LEO satellites have a knowledge of their clock error, this information is not broadcast to the communications network users. Estimating and correcting these errors in SOPs is an ongoing field of research, and is covered in [9, 50, 51, 52, 53].

2.3.3 LEO Network Time

In the precise GPS time transfer techniques of Section 2.1.3, the end goal was to synchronize to GPS Time, which itself is tied to UTC(USNO). To accomplish this, the user applied a satellite clock offset δt^k to the incoming pseudoranges, effectively synchronizing each satellite to GPS Time. The user would then solve for their clock offset δt_u, thereby effectively synchronizing to GPS Time.

The LEO constellation, on the other hand, is not necessarily disciplined to GPS Time like the GPS satellites are to GPS Time. This means the proposed receiver will instead be performing time transfer from another timescale, which is hereafter referred to as network time. A comparison of these two timing paradigms is shown in Figure 2.5. This illustration highlights the difference between GPS and LEO constellation operations. The GPS constellation, shown in Figure 2.5a, receives precise timing information from the ground control segment. This precise time is then transferred to the user via ranging, using the methods presented earlier. The LEO satellite constellation with the proposed shown in Figure 2.5b shows the same type of timing information flow. The satellite network operator monitors satellite clock states, and occasionally corrects them. The designed receiver will then exploit broadcast communications signals to extract this timing information.

Since the receiver in question will be synchronizing with an unknown timescale, two questions must be answered. First, are all of the satellites in the network synchronized accurately enough to network time to be able to perform time transfer to the opportunistic user? Second, is this timescale accurate enough to provide for essential services in the event of a GPS outage? While the answers to these questions most likely vary by constellation, a few inferences can be made.

First, communications inherently requires time synchronization between nodes. Therefore it is reasonable to expect that all satellites on the network will be synchronized to a common time, even if that time is not UTC or GPS Time. For Starlink and Iridium, for example, some level of node synchronization is required because the modulation schemes requires sending data at common times [54, 55]. To accomplish this, the LEO satellites have onboard clocks

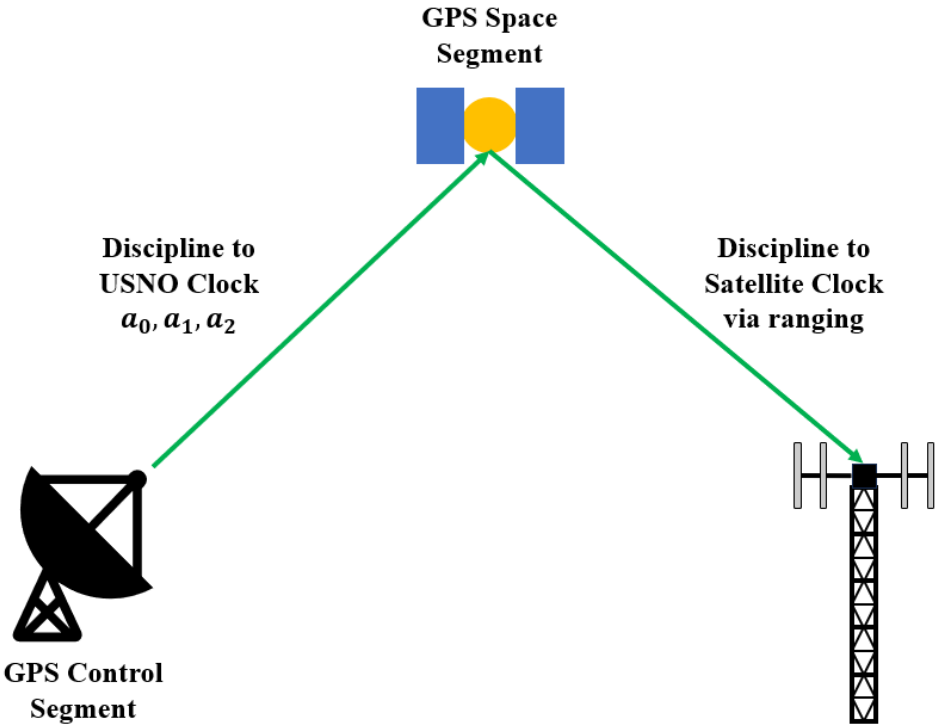

(a) Traditional GPS Time Transfer

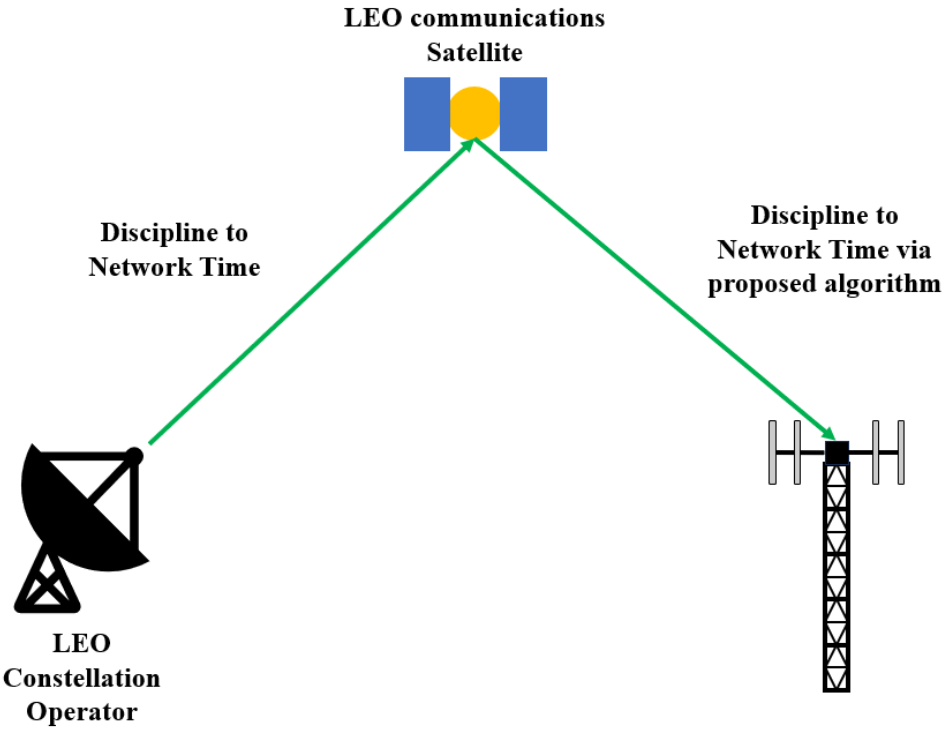

(b) Proposed Receiver Syncing to LEO Network Time

Figure 2.5: Comparison of Traditional Time Transfer to Proposed Receiver

that are tied to GPS Time. However, this does not mean that their transmission times are nanosecond accurate to UTC. For a good example of how node synchronization works for a particular constellation (Iridium), the reader is referred to [52, 53].

This thesis assumes that the opportunistic constellation being tracked has the same synchronization scheme as described in [52, 53]. Namely, that network time is comprised of a static offset from GPS Time and that each satellite's on board clock drifts from network time, requiring periodic corrections to ensure that some maximum deviation from network time is not exceeded. With this assumption in mind, it will be the goal of the proposed receiver to synchronize its internal clock to the network time of the opportunistic constellation, essentially as if it were a node in the network. The constellation's network time is assumed to be of sufficient quality to synchronize an entire network, since that is its purpose. A more detailed description of how this time scale is simulated is presented in the next chapter.

2.4 Conclusion

GPS provides accurate and convenient time transfer capability that is free to all users. The impact of this service is underscored by the explosion of precise time-equipped devices that have become commonplace in almost every industry sector. This importance, combined with GPS' low received power, makes it a potential point of weakness. LEO SOPs are currently being explored as a solution to this weakness, offering signals that can cut through foliage and buildings, and are much harder to interfere with. This technology is limited, however, since it was not designed with precise timing transfer in mind. The emitter locations are unknown, making ranging impossible without estimation of satellite positions. Additionally, emitter clock states have an unknown offset from the desired GPS Time, which must also be estimated. The following chapters discuss how the proposed timing receiver will work through these limitations to provide timing synchronization through LEO network time independent of GPS.

Chapter 3

Proposed Time Transfer Receiver

In order to provide robust timing estimates, this thesis focuses on obtaining timing state estimates from LEO SOPs. This is due to their high signal power and good geometric diversity, making them good compliments and acceptable backups for necessary GPS time. To meet this goal with LEO SOPs, a multi-antenna receiver is proposed that can jointly estimate satellite position and receiver time using a combination of pseudoranges, Doppler shifts, and angles of arrival (AoAs). More precisely, the receiver estimates user clock bias, user clock drift, as well as position and velocity vectors for all satellites overhead. The state vector is given in Equation (3.1).

$$\mathbf{x} = \begin{bmatrix} \delta t_u \\ \dot{\delta} t_u \\ \mathbf{x}^1 \\ \mathbf{x}^2 \\ \vdots \\ \mathbf{x}^k \end{bmatrix} \tag{3.1}$$

In Equation 3.1, $\mathbf{x}^k$ is the state vector of each individual satellite shown in Equation (3.2).

$$\mathbf{x}^k = \begin{bmatrix} x^k \\ y^k \\ z^z \\ \dot{x}^k \\ \dot{y}^k \\ \dot{z}^k \end{bmatrix} \tag{3.2}$$

The rest of this chapter describes the models that the estimator will use to estimate the state vector given in Equation (3.1). Section 3.1 gives an overview of the proposed receiver, detailing its antenna layout and the principle of AoA. Section 3.2 gives an overview of the receiver and the measurements it uses. Models for pseudorange, differenced carrier phase, and Doppler shift are presented. Section 3.3 describes the process of modeling and simulating satellites. Section 3.4 describes the clock model that will be used to simulate the clock bias and drift of both the receiver and the satellite emitters. Section 3.5 outlines how the receiver will use an Iterated Extended Kalman Filter to estimate the states of interest.

3.1 Proposed Timing Solution

The LEO AoA-based receiver layout is shown in Figure 3.1. In this image, the receiver consists of multiple antennas arranged orthogonally in the north-east plane. At each of these antennas, the receiver will make measurements of range to LEO satellites as well as carrier phase measurements. The carrier phase will allow for the calculation of an AoA of the incident signal, and when combined with the range will yield a joint solution for satellite location as well as for receiver timing offset.

In order to obtain AoA to the LEO emitter, a relationship between relative carrier phase and AoA needs to be established. This relationship is shown in Figure 3.2. In this diagram it can be seen that across two antennas, taking the difference of the precise carrier phase range yields one of the sides of a right triangle, highlighted in red in the figure. The hypotenuse

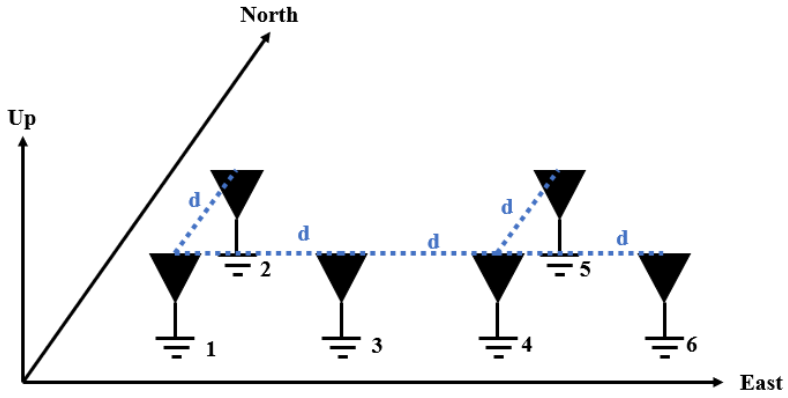

Figure 3.1: Proposed Receiver Layout

of this triangle is the baseline distance between the two antennas where the carrier phases is measured, or d_{ij}. Using trigonometry, the AoA, θ_k, can be calculated with Equation (3.3).

$$\Delta\Phi_{ij}^{k} = d_{ij}cos(\theta_k) \tag{3.3}$$

In this equation, $\Delta\Phi_{ij}^{k}$ is the difference between carrier phases from satellite k taken at antennas i and j. In order to solve for AoA, Equation (3.3) can be rearranged to obtain Equation (3.4).

$$\theta_k = cos^{-1}\left(\frac{\Delta\Phi_{ij}^{k}}{d_{ij}}\right) \tag{3.4}$$

With AoA introduced, the next section introduces the mathematical models for the measurements the proposed receiver will use.

In addition to the antenna layout, several other assumptions are made in this thesis. First, all receiver antennas are assumed to be tied to a common clock. Having all antennas synchronized to local time is important as it ensures that all range measurements have the same clock bias error. If each recording antenna has a separate clock bias, it will be impossible to synchronize the receiver with the measurements described in the next section as there will be too many

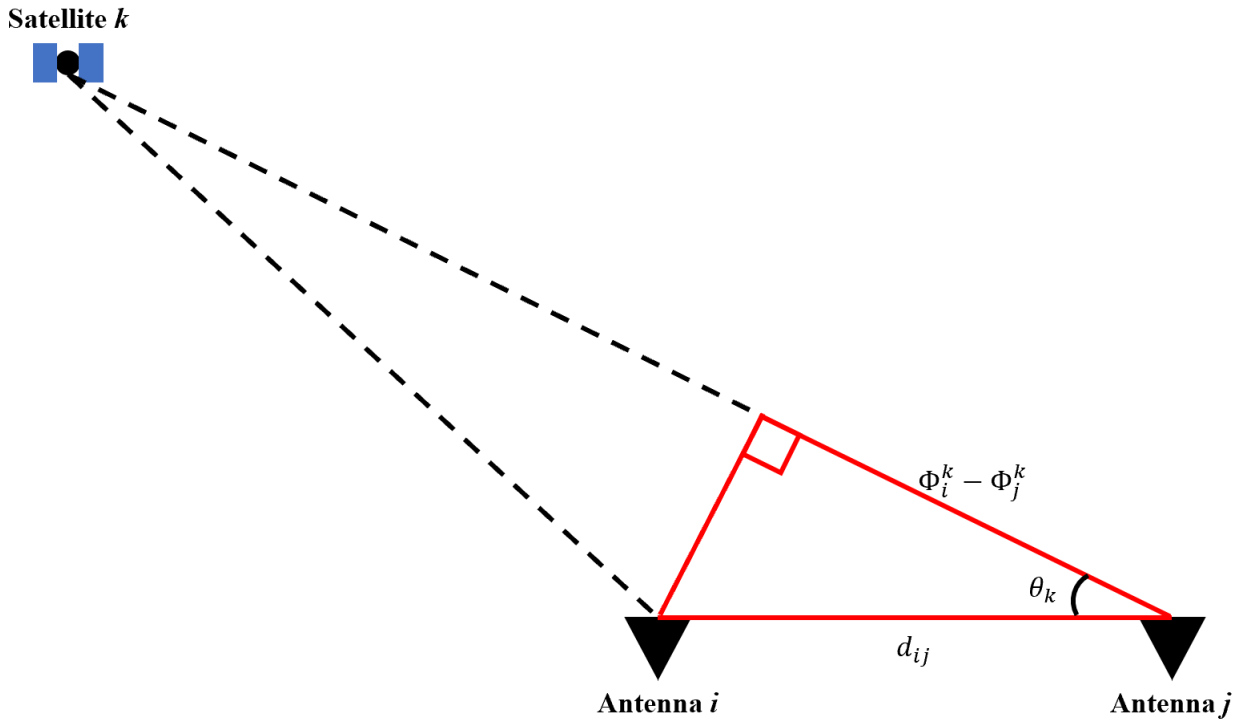

Figure 3.2: LEO AoA Calculation

states to estimate at once. This assumption is also a very reasonable one, as the synchronization signal from a common oscillator can easily be delivered over coax cable.

Second, the antenna platform is assumed to be stationary with respect to the local North-East-Down (NED) reference frame. In the measurement models described in this thesis, it is assumed that an accurate receiver location is known to the estimator at all times. This assumption is only feasible if the receiver is stationary at a surveyed location. This constraint is not overly restrictive, since the operations requiring precise timing that this work seeks to service are all stationary as well.

Third, each of the receiver's antennas are all at known locations. Antenna placement knowledge lowers the number of unknown states in the measurement equations and makes AoA estimation possible. With these assumptions in mind, the next section introduces the measurement model in mathematical detail.

Finally, it is assumed that the receiver has obtained an unambiguous AoA. For the receiver antennas shown in Figure 3.2, ambiguous AoAs arise when the distance between the two receiving antennas (d_{ij}) is greater than a half-wavelength of the carrier. This ambiguity arises

from the unknown number of carrier cycles that lie between the two antenna, and means that multiple angles could represent the true AoA. In order to resolve this issue, this thesis assumes the use of TLE data to constrain and resolve the true AoA. Details on how this is performed are given in Appendix **??**.

3.2 LEO AoA Measurement Model

This section contains a detailed description of the measurement model that will be used to estimate the states of interest. It describes the models for SOP-obtained pseudoranges and AoA measurements. This foundation will allow for the application of a nonlinear estimator to solve for clock offset so that the receiver can synchronize its clock to the LEO constellation.

3.2.1 Pseudoranges

The pseudoranges used by the receiver are assumed to have been obtained opportunistically from LEO satellites. This opportunistic tracking is assumed to have provided a time of flight (TOF), carrier phase, and Doppler shift. Their form, given in Equation (3.5), is similar to that of GPS, as shown below.

$$\tilde{\rho}^k = \sqrt{(x^k - x_u)^2 + (y^k - y_u)^2 + (z^k - z_u)^2} + c\delta t_u + \epsilon \tag{3.5}$$

The primary difference between the LEO pseudorange model and the GPS pseudorange model is the omission of satellite clock error, δt^k. This effectively means that the proposed receiver is not synchronizing to UTC or GPS Time, but to the network timescale of the LEO satellite constellation. This assumption will be explored further in a future section, but a few details can still be noted. First, it is assumed that the LEO network time scale is tied to GPS, meaning that periodic corrections are made such that the network time loosely conforms to GPS Time. This is a reasonable assumption, as it is known that many LEO constellations do indeed synchronize to GPS Time with onboard receivers [53]. Second, the LEO clock type is assumed to be an OCXO [56]. The OCXO provides good stability for short durations, but each satellite will have large offset errors due to the inaccurate oscillator.

Also unlike GPS, each satellite's position (x^k, y^k, z^k) is unknown to the user. These states will be estimated by the receiver. On the other hand, the assumption of a static, known receiver location alleviates having to estimate the user position states, (x_u, y_u, z_u). This highlights why the static assumption is so important to the system, as it lowers the number of unknowns in the measurement model to allow observability.

3.2.2 Differenced Carrier Phase

In Section 3.1, the means by which AoA information assists in state estimation was briefly discussed. This involved taking LEO carrier phase measurements from two different antennas and differencing the measurements. The two individual carrier phase measurements are given in Equations (3.6-3.7).

$$\phi_i^k = -\frac{1}{\lambda}[r_i + I_{\phi_i} + T_{\phi_i}] + \frac{c}{\lambda}\delta t_u + N_i^k + \epsilon_{\phi_i} \tag{3.6}$$

$$\phi_j^k = -\frac{1}{\lambda}[r_j + I_{\phi_j} + T_{\phi_j}] + \frac{c}{\lambda}\delta t_u + N_j^k + \epsilon_{\phi_j} \tag{3.7}$$

Like the SOP-obtained pseudoranges, the transmitter clock bias has been removed from the expression, leaving only the user's clock bias. Taking the difference of these two measurements is advantageous for several reasons. First, because the antennas are close together, subtracting one from the other essentially removes atmospheric error. This is because antennas within several hundred meters of each other will experience approximately the same atmospheric errors. This means that $I_{\phi_i} \approx I_{\phi_j}$ and $T_{\phi_i} \approx T_{\phi_j}$ so they will disappear from the single difference. The same logic applies to the clock biases of the user and the satellite.

Differencing cannot fix the last two terms, however. The carrier phase ambiguities N are not the same between antennas. Many applications involving AoA use antennas spaced less than one half wavelength (λ) apart to remove this constraint. Unfortunately, as will be seen, the high accuracy AoAs required to position LEO satellites demand longer baselines that make this term difficult to estimate. In addition, combining these two measurements will increase the variance, or uncertainty, on the noise terms ϵ_{ϕ_i} and ϵ_{ϕ_j}. While this does degrade measurement quality, the carrier phase measurements are already so precise that a good quality measurement

can still be obtained. The final difference equation is shown in Equation (3.8).

$$\phi_i^k - \phi_j^k = \Delta\phi_{ij}^k = -\frac{1}{\lambda}(r_j - r_i) + (N_i^k - N_j^k) + \epsilon_{\Delta_{ij}} \tag{3.8}$$

In this equation, $\epsilon_{\Delta_{ij}}$ is the new noise term brought on by the subtraction of the two original measurements. While $\Delta\phi_{ij}^k$ is the differenced carrier phase in angular units, it is easier in this case to have differenced carrier phase in distance units. To accomplish this, the entire expression is multiplied by $-\lambda$.

$$\Delta\Phi_{ij}^k = (r_j - r_i) + -\lambda(N_i^k - N_j^k) + -\lambda\epsilon_{\Delta_{ij}} \tag{3.9}$$

The most troublesome term in Equation (3.9) is the difference between the carrier phase ambiguities. Estimating this difference is an ongoing field of research, and is covered in [57, 58]. This thesis assumes that the receiver has employed one of these estimation techniques successfully to obtain the differenced integer, resulting in a measurement described by Equation (3.10).

$$\Delta\Phi_{ij}^k = (r_j - r_i) + \epsilon_{\Delta\Phi_{ij}} \tag{3.10}$$

In this equation, $\epsilon_{\Delta\Phi_{ij}}$ is the system noise expressed in terms of carrier phase in meters. Equation (3.10) is the differenced carrier phase model that will be used in state estimation. In the simulation studies that follow, Equation (3.10) is the exact form that will be used to generate measurements in the sim environment.

While these measurements are adequate for estimating satellite position states, they carry the assumption that the receiver can continuously track the signal to accumulate carrier phase and form a biased range measurement. This assumption is unreasonable for LEO SOPs, as most of the signals do not emit a continuous carrier wave. It has been shown, however, that AoA from non-continuous LEO signals can still be estimated [59, 60]. For this reason, the AoA measurement in Equation (3.3) must be modified to be in terms of the states of interest.

In order to get Equation (3.3) in terms of the Cartesian satellite states that are to be estimated, the AoA is rewritten using the definition of the dot product. Doing so expresses the

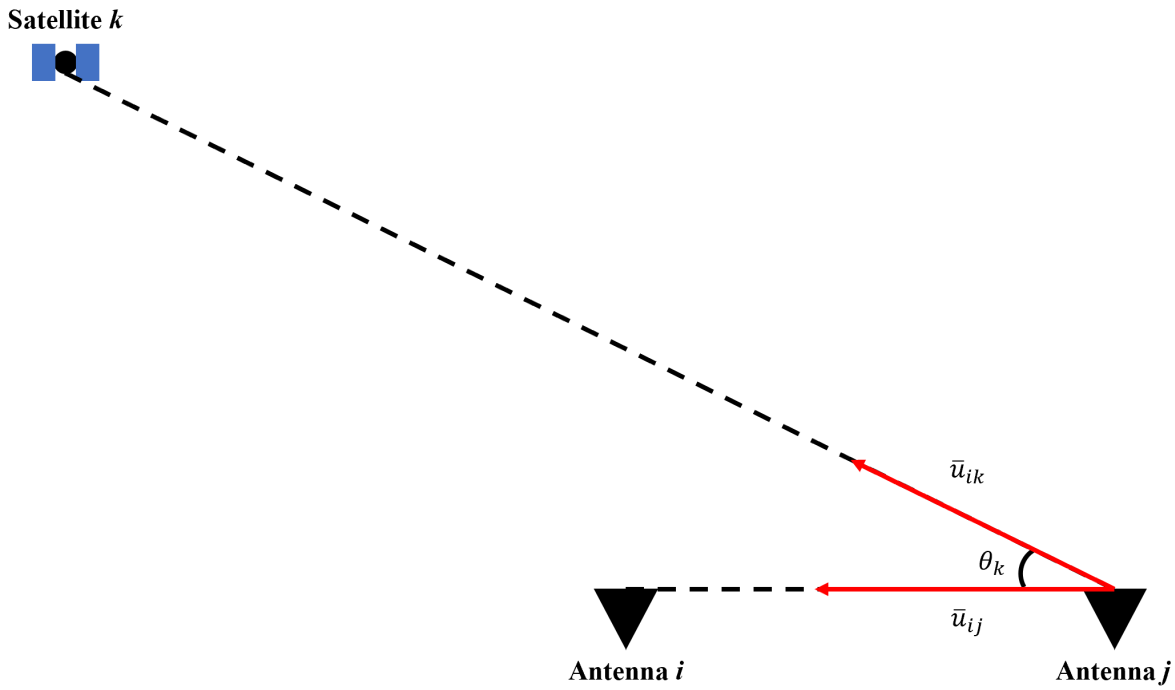

Figure 3.3: AoA expressed with unit vectors

angular term by its pointing vector mathematical equivalent. Equation (3.11) shows the relationship used.

$$\bar{a} \cdot \bar{b} = |\bar{a}||\bar{b}|cos(\theta) \tag{3.11}$$

The dot product between two vectors is equivalent to their vector magnitudes multiplied together and multiplied by the cosine of the interior angle between them. In this case, the angle represents an angle formed between the antenna baseline and the line connecting one antenna (hereafter the primary) to the satellite. This relationship is visualized in Figure 3.3. In this image, $\bar{u}_{ij}$ is the unit vector pointing from antenna i to antenna j, and $\bar{u}_{ik}$ is the unit vector pointing from antenna i to emitter k.

The reason these vectors are given unit magnitudes is so that the magnitude term $|\bar{a}||\bar{b}|$ in Equation (3.11) will be equal to one. This means:

$$\bar{u}_{ij} \cdot \bar{u}_{ik} = cos(\theta_k) \tag{3.12}$$

Substituting Equation (3.12) into Equation (3.3) yields a form of the differenced carrier phase measurement that is clearly related to the satellite states.

$$\Delta\Phi_{ij}^{k} = d_{ij}(\bar{u}_{ij} \cdot \bar{u}_{ik}) + \epsilon_{\Delta\Phi_{ij}} \tag{3.13}$$

The relationship to satellite position present in Equation (3.13) is highlighted by expanding the dot product.

$$\Delta\Phi_{ij}^{k} = d_{ij}\frac{u_{ij,x}(x^k - x_i) + u_{ij,y}(y^k - y_i) + u_{ij,z}(z^k - z_i)}{r_{ik}} + \epsilon_{\Delta\Phi_{ij}} \tag{3.14}$$

In Equation (3.14), $u_{ij,x}$ is the x-component of $\bar{u}_{ij}$, and so on for the other components. r_{ik} is the geometric range from antenna i to satellite k. Taking the partial derivative of this expression with respect to Cartesian satellite states is relatively straight forward, therefore this is a convenient form of the measurement model to apply to the estimator.

3.2.3 Doppler Shift

While pseudorange works to constrain satellite position and user clock bias, Doppler shift measurements are related to satellite velocity and user clock drift. Doppler shift is proportional to range rate by the known wavelength of the signal, λ. Equation (3.15) shows the opportunistic Doppler shift model used in this research.

$$\dot{\rho}^{k} = \dot{r}^{k} + c\dot{\delta}t_u + \epsilon_{\dot{\phi}}^{k} \tag{3.15}$$

Satellite clock drift is considered negligible over the Doppler observation interval, leaving only the true range rate, user clock drift, and errors all lumped into one term. Doppler shift is often the most reliable measurement in SOP positioning systems [61, 62]. Here, the Doppler will be used to jointly estimate user clock offset and the satellite velocity term present in $\dot{r}^{k}$.

Figure 3.4: Logos of LEO Satellite Communications Networks

3.3 Satellite Modeling

Satellite simulation and modeling is performed to assure that the results from this study are as accurate as possible. This section will describe how satellite positions and velocities are generated for the simulator so that the measurement models of Section 3.2 can be applied. For this thesis, LEO TLE data collection and orbit propagation was carried out with the open source navsim Python package, available on GitHub [63]. The following sections describe some of the LEO constellations that can be simulated, how their orbits are propagated through time, and how their network time scales are simulated.

3.3.1 LEO Constellations

There are many satellite constellations in low Earth orbit, and even more planned to launch in the future. Figure 3.4 shows several examples of companies that have launched or intend to launch large scale LEO satellite communications networks into orbit. Orbcomm and Iridium are legacy networks that began launching in the 1990's. Their goals were to allow limited voice and text capabilities to a few subscribed users, with a market emphasis for operation where telephone service was unavailable. In recent years, Iridium has updated their constellation with new satellites and a navigation signal [64, 20].

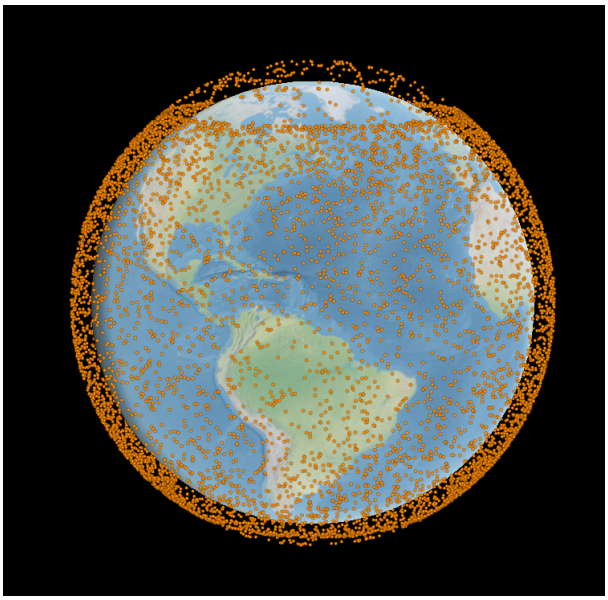

Figure 3.5: Current Operational Starlink Satellites, courtesy of AstriaGraph [66]

OneWeb and Starlink, on the other hand, represent the future of LEO satellite communications. These companies aim to provide broadband internet service for worldwide subscribers, which requires higher throughput and more backhaul infrastructure. This means more satellites are required for successful operation and service delivery. As of the time of writing, Starlink has launched over 6,200 communications satellites into orbit, with more planned [65]. An image of all current Starlink satellites is shown in Figure 3.5, provided by [66]. OneWeb currently has over 630 satellites in orbit, providing the same worldwide coverage as Starlink using higher altitude satellites.

For the opportunistic user, these additional signals and satellite vehicles hold much potential. Additional satellites mean better geometric diversity, and lower orbital altitudes mean higher received power [5]. However, unlike their PNT counterparts in MEO, these LEO mega-constellation satellites are cheaply made and generally less suitable for navigation. The challenges of using these emitters for navigation was discussed in the previous chapter.

3.3.2 Orbit Propagation

This section describes how orbital positions for the LEO satellites are simulated in software. The proposed receiver will use AoA and pseudoranges to solve for satellite position, but truth

positions must be simulated and fed into the simulation environment. The navsim python software package was used to generate these truth positions using TLE data. As was discussed previously, TLE data contains ephemeris information for LEO satellites that is inaccurate for navigation purposes. This thesis uses TLE data to simulate truth positions that behave in a manner consistent with satellite orbital motion.

With orbital elements provided by TLEs, navsim uses an orbital propagation model called Simplified General Perturbations 4 (SGP4). SGP4 was developed in the 1970's as a tool to help NORAD track objects in orbit [67]. Error growth in these solutions is on the order of kilometers per day, so they are updated frequently by the North American Aerospace Defense Command [10]. Nevertheless, the positions are not precise enough for precise time synchronization, and thus are still estimated in the simulation environment.

3.3.3 Constellation Network Time

As discussed in Section 2.3.3, the LEO satellite communication nodes that are being used for opportunistic time transfer are assumed to be on network time. Network time in this case is assumed to be offset from GPS Time, with tolerable errors much larger than GPS Time [52, 53]. The constellation clocks are modeled by the two state clock model, described in the Section 3.4. It is assumed that when these clocks deviate from the network time standard by some threshold, it is detected by a monitoring station and corrected.

This behavior model of LEO satellites has been observed experimentally using the Iridium constellation [52, 53]. Pratt et. al realized a satellite clock bias estimator for Iridium, demonstrating that real LEO satellites exhibit this behavior. Figure 3.6 from [52] shows the clock motion of 11 Iridium satellites for a 24 hour period starting on December 16, 2011.

To simulate the clock dynamics shown in Figure 3.6, simulated satellites were equipped with OCXO clocks. The satellites are simulated to have a maximum clock error from LEO network time of 2μs, which is the maximum deviation before correction observed in Figure 3.6. When the nodes drift past this time accuracy, a random correction is issued that places the node's clock back in the acceptable operating range. Simulations where the LEO satellites' drift was constrained by the ground station were not considered.

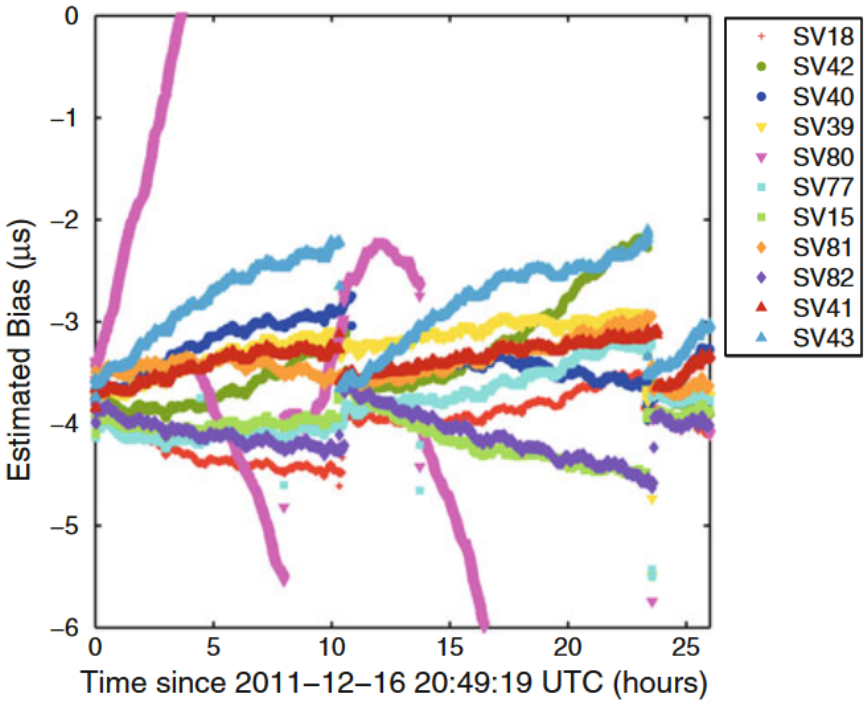

Figure 3.6: Example of LEO Network Time [52]

The assumption that the satellites in the network be on a common time scale is crucial to operating the proposed receiver. This assumption implies that the zero mean random walk processes that govern the satellite clocks will average out to the network time across all nodes. This fact is exploited by Equation (3.5), when it is assumed that all satellites are on network time.

3.4 Clock Modeling

In the preceding sections, time transfer to GPS Time or network time was accomplished by solving for a local clock bias, δt_u. This clock bias is never a constant value, and the drift it exhibits over time must be simulated. The model used in this research to simulate clock offset and drift is called the two state clock model, and is covered in [68]. In this model, the bias takes the form of a set of differential equations, with clock errors arising from Brownian motion and additive white noise.

3.4.1 Two State Clock Model

Clocks have two primary components, an oscillator and a counting circuit (i.e., a shift register), both of which are modeled using the two state clock model. The oscillator generates a periodic signal, and cycles of this signal are counted to give a measurement of time. The error in a clock arises from imperfections in the oscillator, causing deviations in clock phase. Galleani's expression for frequency deviation (clock drift) is shown in Equation (3.16) [68].

$$f_{dev}(t) = \zeta_1 + \int_0^t \zeta_2 \, dt \tag{3.16}$$

In this equation, ζ_1 and ζ_2 are zero-mean white noise sources.

$$\zeta_1 \sim \mathcal{N}(0, \sigma_{\zeta_1^2}) \tag{3.17}$$

$$\zeta_2 \sim \mathcal{N}(0, \sigma_{\zeta_2^2}) \tag{3.18}$$

Similarly, phase deviation (clock bias) is obtained by integrating frequency deviation.

$$\phi_{dev}(t) = \int_0^t f_{dev}(t) \, dt \tag{3.19}$$

ζ_2 is white noise that is integrated to produce the frequency deviation in Equation (3.16). Clocks that have a low ζ_2 are therefore said to have good frequency stability. On the other hand, ζ_1 is white noise that is integrated and added to the frequency deviation. Clocks that have a low value for ζ_1 are said to have good phase stability.

An overview of clock bias simulation and associated terms is shown in Figure 3.7. In order to simulate according to the diagram in Figure 3.7, power spectral densities (PSDs) for ζ_1 and ζ_2 are needed. These values are experimentally obtained with a statistical tool called the Allan Variance, which is described in the next section.

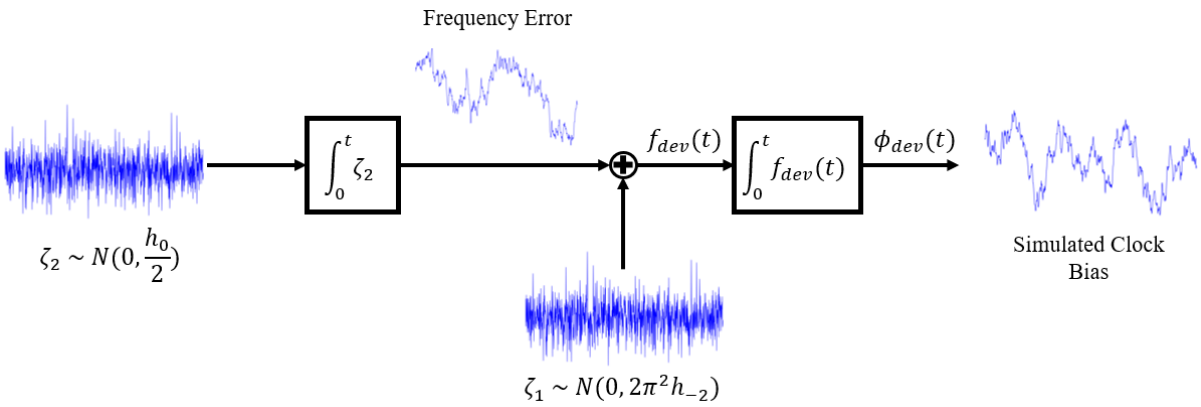

Figure 3.7: Two State Clock Model Simulation

3.4.2 Allan Variance

The Allan Variance (AVAR), first proposed by David Allan, is a tool used to measure the deviation of a random walk process [69]. A good description of the algorithm and its resulting usage in estimators is given in [70]. The Allan Variance is shown in Equation (3.20).

$$\sigma_y^2(\tau) = \frac{1}{2} E\left[(\bar{Y}_{k+1} - \bar{Y}_k)^2\right] \tag{3.20}$$

In this Equation, τ represents a time window of the signal y. The expression for $\bar{Y}_k$ is given in Equation (3.21).

$$\bar{Y}_k = \frac{1}{\tau} \int_{t_k}^{t_{k+1}} y(t)\, dt \tag{3.21}$$

The Allan Variance, then, splits the signal $y(t)$ into segments of length τ, integrates each segment, and takes the variance of all integrated segments. The output is a series of variances that is plotted against window length that can tell a great deal about the underlying noise that is driving the process. Two Allan Variances are shown in Figure 3.8, one for a high quality rubidium atomic clock and one for a low quality TCXO.

The atomic clock's Allan Deviation shown in Figure 3.8a has a 'V' shape, each part of which has a mathematical interpretation. The left side of the 'V' is a logarithmic descent, indicating the presence of an additive zero mean noise source, which is known to be the phase noise in Equation (3.16). The right side of the plot shows an increase in the deviation after a certain point. This increase is due to the integrated frequency noise in Equation (3.16). The

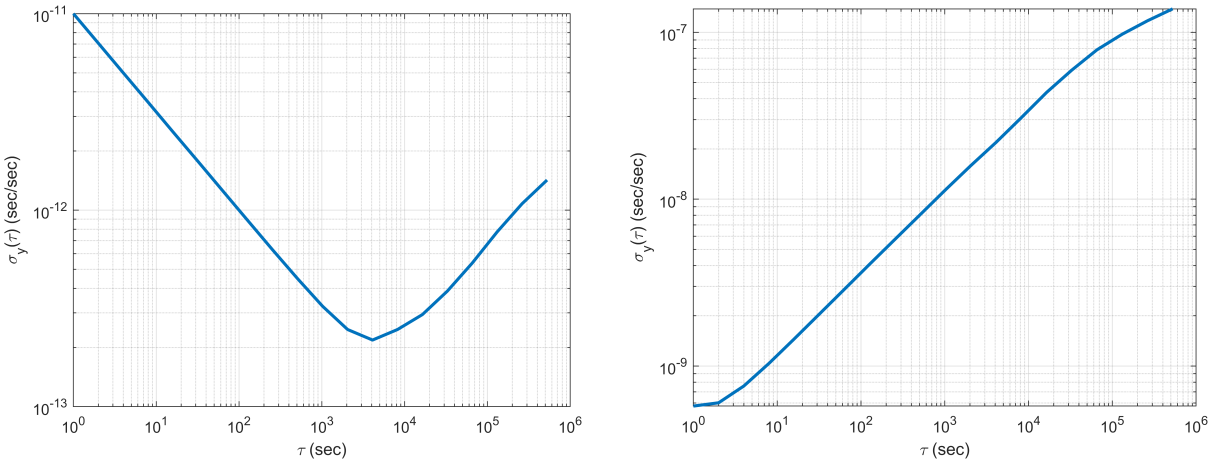

(a) Simulated Rubidium Standard

(b) Simulated TCXO Standard

Figure 3.8: Allan Deviation of Two Clocks' Frequency Stability

Allan Variance plots of this oscillator shows that for increasing averaging times up to a point, performance can be improved drastically.

The TCXO Allan Variance in Figure 3.8b, on the other hand, exhibits much different behavior. The monotonically increasing line shows that the TCXO's clock drift is strictly increasing over time, indicating poor frequency and phase stability. The information from Allan Variance plots is used to characterize the behavior of oscillators, simulate their errors, and inform covariances of estimators. The noise values used to generate these Allan Variance plots and the actual noise used in simulation were taken from the following table given in [71].

Table 3.1: Clock Noise Parameters, taken from [71]

Clock Grade	h_0	h_2
Low Quality TCXO	$2e^{-19}$	$2e^{-20}$
High Quality TCXO	$2e^{-21}$	$2e^{-20}$
OCXO	$2e^{-25}$	$6e^{-25}$
Rubidium	$2e^{-22}$	$1e^{-30}$

3.5 Estimator Design

The receiver must estimate the state vector of Equation (3.1) using the measurement models and dynamic state models that have been outlined. One such state estimation method is the Kalman Filter (KF). This section outlines the working principles of the KF, as well as the particular KF variant that was employed in this research, the Iterated Extended Kalman Filter (IEKF).

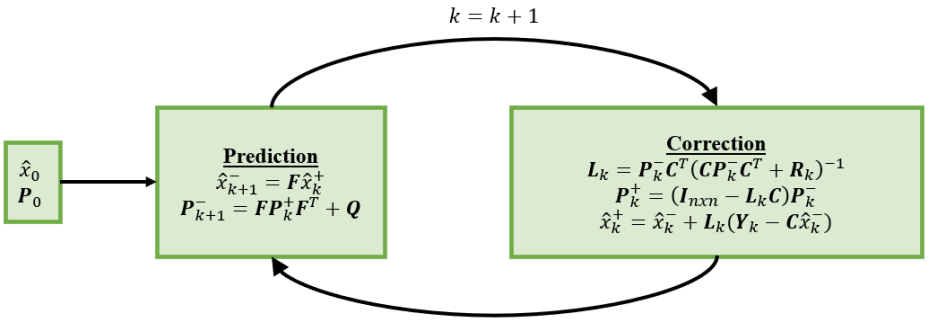

Figure 3.9: A Basic Kalman Filter

3.5.1 Kalman Filter

The Kalman Filter is a linear estimation algorithm used for observing dynamic states. Given a model of a dynamic system and imperfect measurements of the states the model describes, the Kalman Filter will return an optimal estimate of the value of the states and the uncertainty of its prediction. Figure 3.9 shows the algorithm in block diagram form. An initial state estimate $\hat{x}_0$ and an initial state covariance matrix $\mathbf{P}_0$ are used to propagate the state estimates and state covariance forward in time using the dynamic model on the left side of the diagram. After prediction, the Kalman Filter receives a measurement of the states and executes the correction equations, shown on the right of the diagram. The correction step serves to form an optimal estimate

The Kalman Filter is effective, but it requires that the system equations of motion as well as the observation equations be linear. In practice, most physically realizable systems exhibit non-linear behavior, rendering the Kalman Filter impractical for many applications. An augmented version of the Kalman Filter, the Extended Kalman Filter (EKF) approximates nonlinear terms using a first order Taylor Series expansion. While suitable for many nonlinear systems, the EKF still relies on the assumption that the linear approximation provided by the Taylor Series be locally valid, which is not always the case.

An EKF was attempted in early stages of research but failed to constrain the state estimates. The reason for failure is that the linear approximations of the measurement equations were not accurate enough, causing state estimates to diverge from truth. For this reason, an

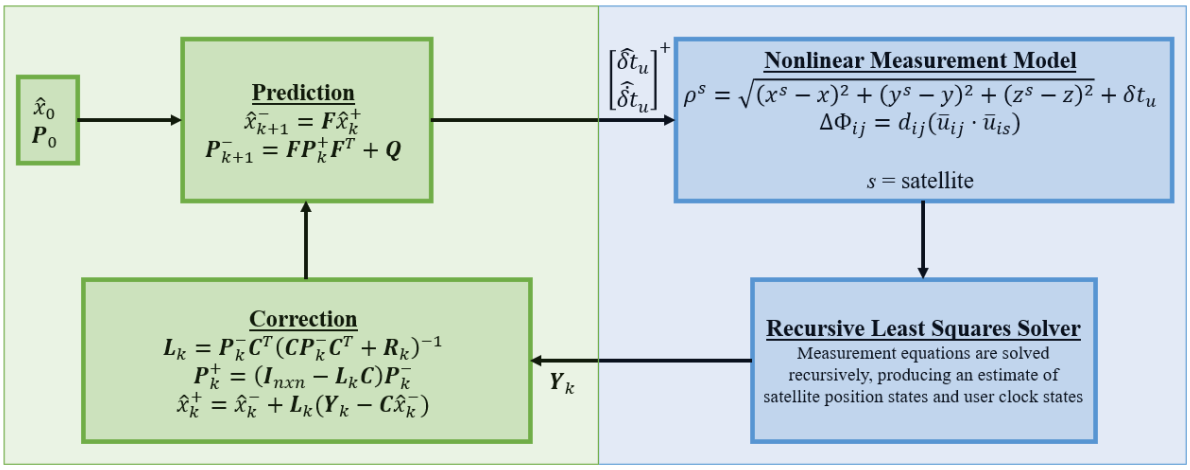

Figure 3.10: IEKF Framework

EKF adaptation known as the Iterated Extended Kalman Filter (IEKF) was employed, which is described below.

3.5.2 Iterated Extended Kalman Filter

The IEKF is a filtering technique that solves system nonlinearities with recursive solution techniques. Recursive solvers for nonlinear functions is a well studied field of mathematics, and the IEKF applies this knowledge to the time domain filtering problem of the EKF. The IEKF used in this thesis is shown in Figure 3.10. The left side of the diagram in green shows the Kalman Filter Equations, while the right side in blue details the solution to the nonlinear measurements.

Overall, the goal of the receiver is to estimate the state vector in Equation (3.1). The IEKF shown in Figure 3.10, however, tracks only two states, shown in Equation (3.22).

$$\mathbf{x}_{IEKF} = \begin{bmatrix} \delta t_u \\ \dot{\delta} t_u \end{bmatrix} \tag{3.22}$$

Tracking only clock bias and drift allows for a KF to be employed. The state transition matrix $\mathbf{F}$ is a discrete time constant velocity model, and the process noise model $\mathbf{Q}$ is taken from the two state clock model in Section 3.4 [68]. After prediction, the KF passes its prediction of clock states into the nonlinear measurement model. The complete state vector from

Equation (3.1) is estimated from the measurements using recursive least squares. When a satisfactory solution has been found, the least squares estimate of clock bias and drift is passed to the Kalman Filter to act as a direct measurement of the states. Additionally, the solver also returns the covariance of its estimate, which is treated as the measurement noise matrix $\mathbf{R}$ in the correction step of the KF.

3.6 Conclusion

This chapter introduced the proposed solution to holdover precise timing in a GPS outage. Its working principle is to use opportunistic ranges and AoA from LEO satellites of unknown location to estimate the unknown satellite states and user clock bias states simultaneously. In order estimate satellite position with AoA measurements, the multiple antennas used by the receiver must be in a set configuration and at a position fully known by the user. The state vector to be estimated and the measurement models were introduced mathematically, and models for satellite motion were specified. The LEO constellation network time that the receiver will synchronize to is presented and simulated. A simple two state model of clock drift and phase motion was introduced, and the importance of the Allan Variance as a statistical tool to analyze random walk processes was detailed. Finally, the IEKF estimator was introduced to produce timing estimates from the collected measurements. The next chapter explains an experimental study performed to characterize the noise profiles of real SOPs to further enhance the realism of the simulation.

Chapter 4

Experimental SOP Error Study

This thesis describes a simulation study where LEO communications satellites are used for timing synchronization. In order for these results to be realistic, the simulation must have an accurate knowledge of the errors that should be applied to received measurements. While closed form models for the probability density functions of noise from traditional GNSS tracking exist, these models cannot be used for SOP timing. This is due to the fact that SOPs are not tracked in the same way GNSS are, since SOP's signal structure is not usually known.

To overcome this limitation, this chapter describes a process for obtaining an empirical noise model from real collected ranges. The ranges come from Iridium LEO communications satellites, and are collected with a Jackson Labs Iridium STL receiver. These ranges are collected and compared to STL broadcast satellite positions and a surveyed antenna location. A polynomial fit is applied to the resulting error to remove the mean arising from the various biases in the system. Finally, a noise model is calculated. This process is performed on both pseudorange and Doppler shift measurements.

4.1 Experimental Data Collection

A diagram of the experimental setup used in this process is shown in Figure 4.1. The two inputs are an antenna and time source. The antenna used in this work is atop the Auburn University MRI Research Center on Devall Drive in Auburn, Alabama. It is static, well surveyed, and has an unobstructed view of the sky. This antenna provides input to a Jackson Labs STL-2600 receiver designed to use the Iridium STL signal. The second input is a Stanford Research Systems Precise Rubidium Standard (PRS10). It has an advertised holdover accuracy of 72 hours,

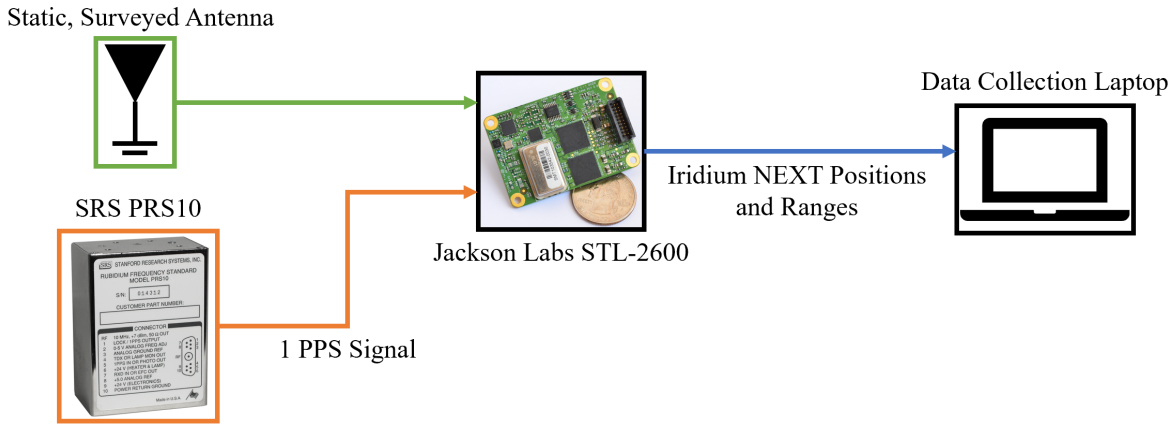

Figure 4.1: Experimental Setup for STL Range Noise Characterization

meaning that in the absence of GPS it will maintain sufficient timing accuracy for telecommunications for 3 days [72]. The PRS10's 1 Pulse Per Second (PPS) output in free running mode provides a reference to the STL receiver. The data collection laptop was running the Ubuntu operating system. The ROS software package was used to collect satellite positions from the Jackson Labs, with all satellite positions being timestamped to the computer's system time.

To assess the accuracy of STL ranging, truth ranges were calculated based off the precisely known location of the receiver antenna and the broadcast Iridium satellite positions recorded from the Jackson Labs receiver. This information was used to calculate a geometric range, which was then compared to the range output from the receiver itself. With publicly available information, this is the most precise range that can be constructed to the Iridium satellite vehicles, making it the truth source for the experiment.

4.2 Iridium STL Ranges

This section details the specifics of the STL ranges that were collected, and how bias errors were removed. In addition, the process for fitting and removing the remaining errors is described, and the final noise model is presented in Appendix B. This effort allows for more precise simulation to add validity to the results of the next chapter.

4.2.1 Range Dataset

The goal of this analysis is to determine a noise model for Iridium pseudoranges and Doppler shifts. The first step in this process was to determine the true ranges over the experimental interval. This was done by taking the vector distance from the surveyed antenna to the Iridium satellite positions from the Jackson Labs receiver. It should be noted that the Jackson Labs receiver does not have perfect knowledge of the satellite states, but it is expected that the error that this introduces is small compared to the error that the ranges will exhibit. Additionally, since this error is likely the result of inaccurate ephemeris information in the STL system, these errors should appear to be slowly changing biases, and thus will be dealt with at a later processing step.

Figure 4.2 gives an overview of the true calculated ranges and the STL ranges. On the left, Figure 4.2a shows the true ranges to the satellite that were being tracked by the Jackson Labs receiver during this particular experiment, which lasted almost 10 minutes on July 27, 2024 starting at 2:26 in the afternoon. The Jackson Labs receiver obtained measurements from 5 Iridium satellites, with Iridium 33 getting the closest to the antenna.

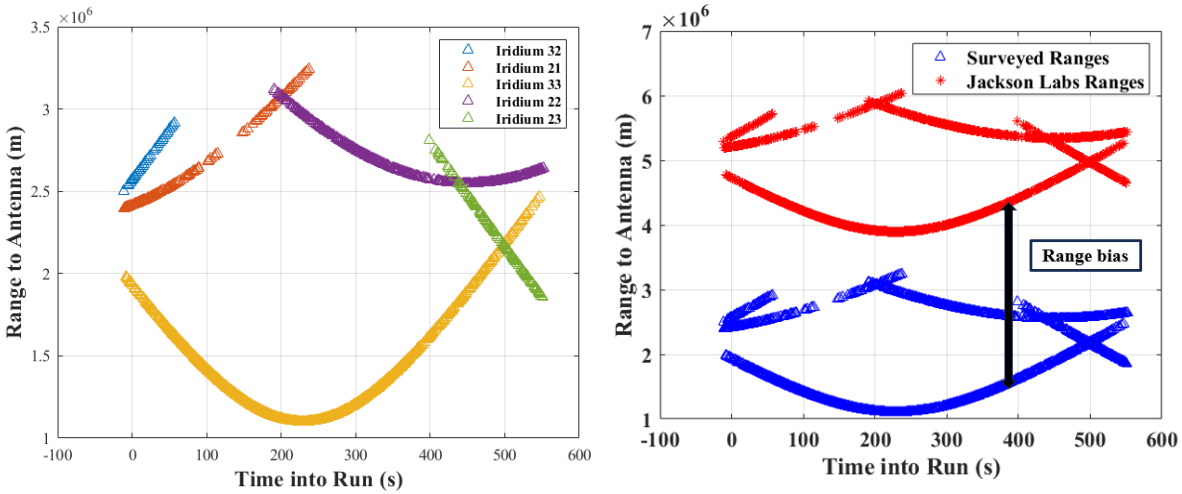

(a) Truth Iridium Satellite Ranges

(b) Biased STL Ranges

Figure 4.2: Collection of Biased STL Ranges

Figure 4.2b on the right compares these truth ranges to STL ranges collected over the same interval. The STL ranges follow the same trends as the truth ranges, but exhibit a clear bias on the order of milliseconds. This offset arises because of user clock bias, satellite clock bias,

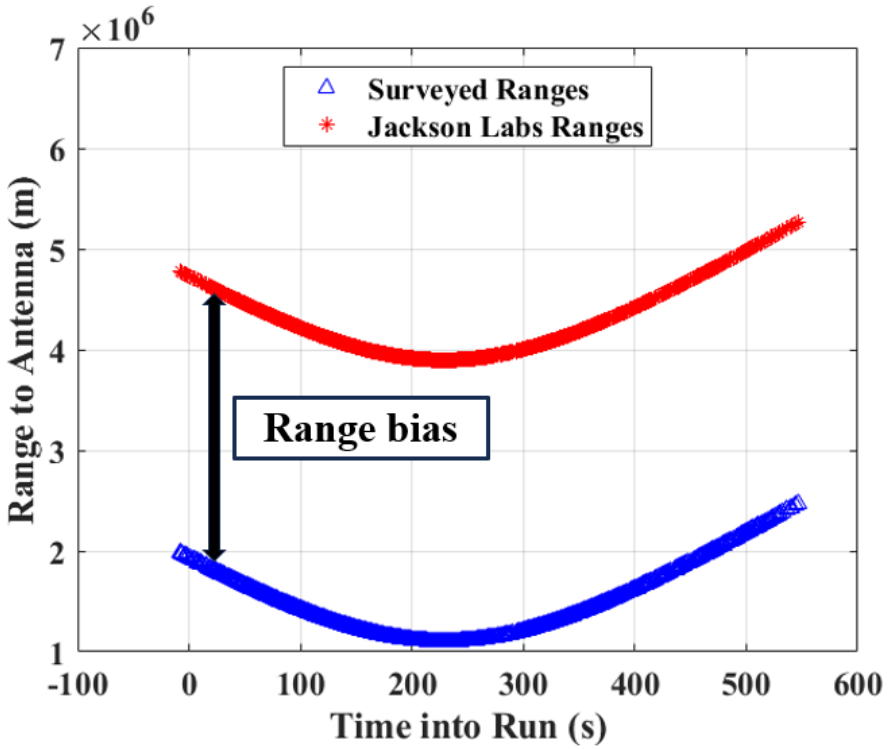

Figure 4.3: Iridium 33 Biased STL Ranges

atmospheric bias, and satellite ephemeris error, with the clock biases making up the majority of the offset. The proposed receiver is designed to estimate these biases. To generate a noise profile for estimation, these biases are manually subtracted so that the underlying noise can be analyzed.

Each satellite has a unique clock bias and different ephemeris and atmospheric errors from the other satellites, so each range bias will be unique. Visually, they all appear to be identical since the common user clock bias is the largest contributor by far, but to accurately gauge the noise, the ranges must be analyzed on a satellite-by-satellite basis. Figure 4.3 demonstrates this process. The surveyed ranges in Figure 4.3 are interpolated to the sample times of the STL ranges using a cubic spline interpolation. Even though the ranges have a mostly similar shape, the large, gradually oscillating error indicates the presence of slowly moving biases in the data. These biases are due to receiver clock bias, receiver clock drift, satellite position error, antenna position error, and atmospheric effects.

Since the goal of this study is to characterize the underlying white noise component of the noise in Figure 4.3, the biases in the data are estimated with a second order polynomial fit.

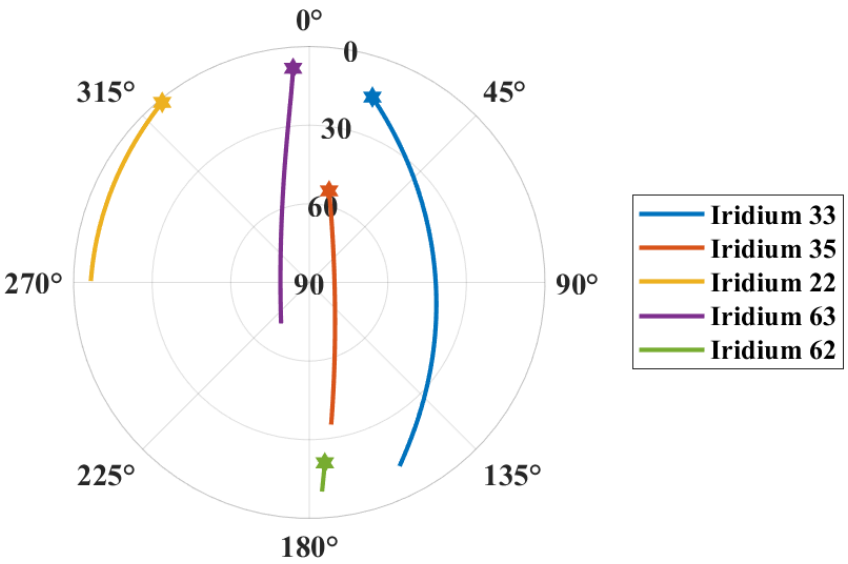

Figure 4.4: Sky Plot of Three Satellites used in Noise Model Fitting

To be able to robustly fit the bias of an arbitrary error profile, the data is divided into shorter time intervals such that a second order polynomial fit is valid over the chosen interval. This is preferable to increasing the fit order, as doing so would tend to fit the noise in the system. The batched method used in this research maintains the benefits of low fit order without sacrificing accuracy.

This process was repeated for twelve additional satellites, with consistent results for each. Data was collected for Iridium satellites that passed overhead, so that there was representative data for almost every elevation angle in the noise fit. It is important that the noise model be merely interpolating from the available data, and not be extrapolating any information. For reference, a sky plot showing the trajectories of five of these satellites is shown in Figure 4.4. Descriptions of the developed noise model from Iridium pseudoranges is given in Appendix B.

4.3 Iridium STL Doppler Shifts

This section details the specifics of the STL Doppler shift measurements that were collected, and how drift errors were removed. In addition, the process for fitting and removing the remaining errors is described, and the final noise model is presented in Appendix B. This effort complements the range noise estimation of the previous section by using the same satellites and datasets.

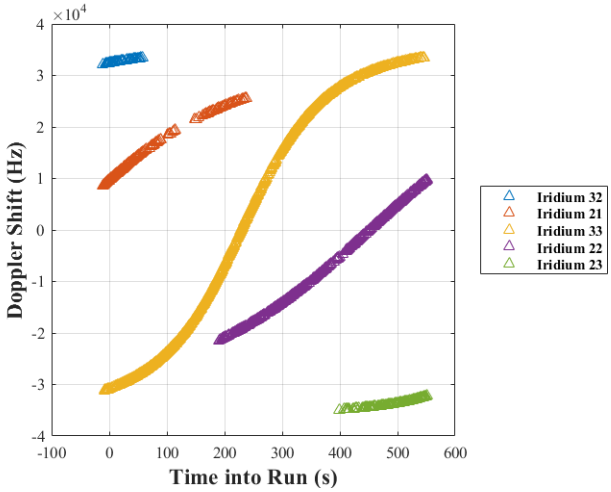

(a) Truth Iridium Satellite Doppler Shifts

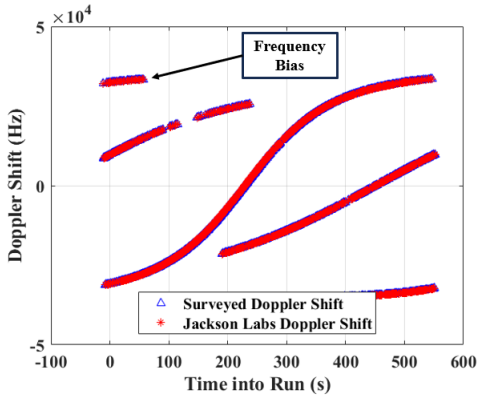

(b) Biased STL Doppler Shifts

Figure 4.5: Collection of Biased, STL Doppler Shifts

4.3.1 Doppler Shift Dataset

Similarly to the pseudorange analysis, the first step is to determine the true Doppler shifts over the experimental interval. To do this, true satellite velocities were recorded over the test interval. Since the antenna is known to be static, the direct relationship between satellite velocity and Doppler shift can be used to calculate a truth Doppler shift.

Figure 4.5 gives an overview of the true calculated Doppler shifts and the STL measured Doppler Shifts. On the left, Figure 4.5a shows true Dopplers from the satellites that were being tracked by the Jackson Labs receiver during one of the experiments. The satellites captured on this recording demonstrate nearly the full range of Doppler shifts possible between a stationary ground user and the Iridium network. Figure 4.5b on the right compares these truth Doppler shifts to measured STL Doppler shifts over the same interval. The STL Dopplers follow the trend of the true Dopplers, just like the range example shown earlier. This time, however, the bias is due to clock drift error in the Jackson Labs receiver. These biases are manually subtracted so that the underlying noise can be analyzed.

Just like range bias, each of the Doppler shift biases shown is unique to each satellite. However, since the Jackson Labs' reference is a very stable Rubidium oscillator, the two Doppler curves appear visually overlaid. Figure 4.6 shows the measured and calculated Doppler shifts for the same Iridium satellite shown in Figure 4.3. Just as before, the calculated Doppler

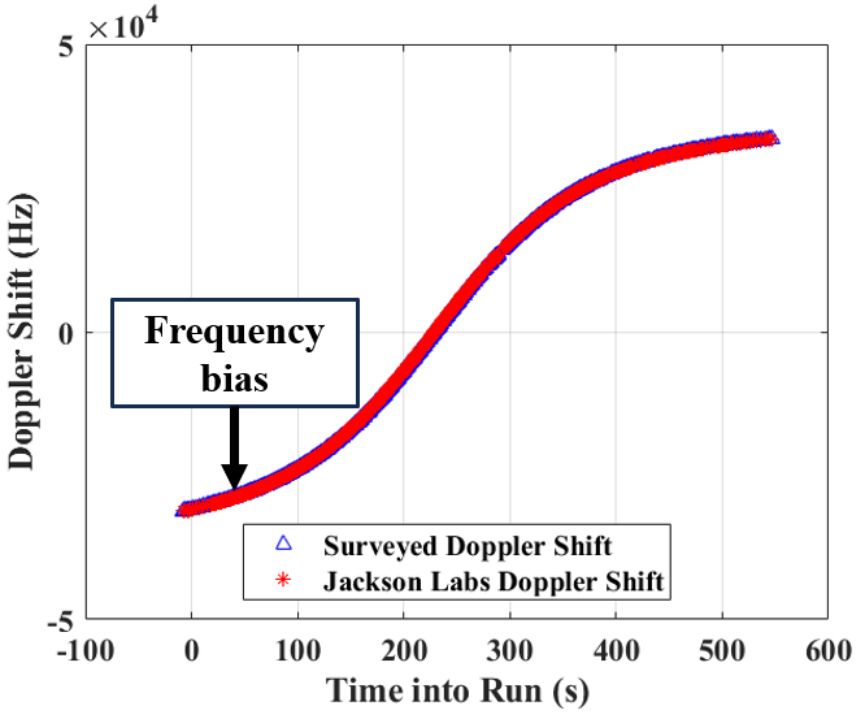

Figure 4.6: Iridium 33 Biased STL Dopplers

shift was interpolated to the STL Doppler sample times. Any resulting error is due to clock drift, atmospheric effects, and satellite velocity errors. These errors are fit with a second order polynomial over intervals of the data, revealing the unbiased underlying white noise. The model error statistics obtained using this data is shown in Appendix B.

4.4 Conclusion

This chapter outlined an experimental study performed to build an Iridium STL range and Doppler shift noise model. The experiment was based off tracking Iridium NEXT satellites, with verification information being provided by a Jackson Labs STL2600 receiver. After conditioning and bias removal, pseudoranges and Doppler shifts from fifteen satellites were combined into a single dataset. This dataset was used to characterize pseudorange and Doppler noise models as a function of satellite elevation. This information will be used in the simulation environment to test the design of the proposed receiver in the next chapter.

Chapter 5

Simulation Results

This chapter describes the simulation results of testing the proposed LEO timing system. Monte Carlo (MC) simulations were performed to assess the receiver's ability to track clock bias and drift from LEO network time. The parameters varied in these simulations are receiver antenna baseline distance and receiver clock grade. Since longer antenna baselines generally yield more accurate AoAs, it is expected that receivers with longer baselines will have more accurate timing estimates [73]. Additionally, clock grade is believed to affect receiver performance as higher quality clocks can maintain better accuracy over longer periods of time. Higher quality clocks have smaller prediction uncertainties, meaning the IEKF discussed in Chapter 3 will be able to track their states more effectively.

The target accuracy of the receiver is 1μs, which is sufficient for telecommunications and power grid management [36]. In order to quantify whether this has been achieved, the filter will be evaluated based on whether its 3σ accuracy is better than 1μs. The 3σ benchmark ensures 99.7% confidence in the timing solution. The rest of this chapter is organized as follows. Section 5.1 describes the test scenarios the receiver was placed under, filter initialization, and the simulation design. Section 5.2 shows results for all tests, comparing their results to the 1μs benchmark which is the target accuracy.

5.1 Monte Carlo Simulation Description

This section outlines the simulation setup used to evaluate the receiver. It describes the software setup, which consists of a Python environment powered by the navsim simulation engine. The

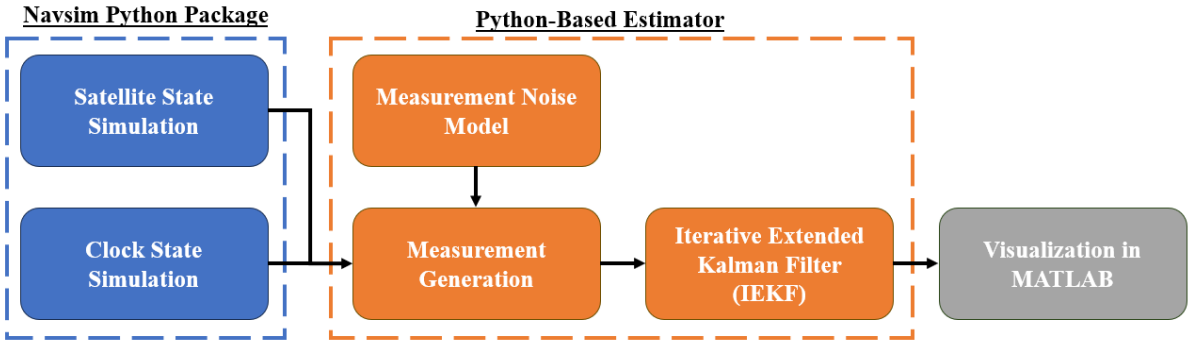

Figure 5.1: Simulator Framework for Estimation

Iterated Extended Kalman Filter (IEKF) initialization setup is discussed, and a testing matrix of receiver configurations is established. These configurations are evaluated in an MC simulation to verify solution accuracy.

5.1.1 Software Setup

The software framework used to evaluate the receiver is shown in Figure 5.1. As was previously mentioned, the navsim Python package was used to simulate satellite position states, satellite clock states, and user clock states. The receiver truth position was known to the receiver, which was simulated in Auburn, AL. Satellite position simulation was carrier out with TLE data files as described previously in Section 3.3. Clocks were simulated using the two state clock model presented in Section 3.4.

The measurement noise model used in this research was derived in Chapter 4. This involved collecting pseudoranges and Doppler shift measurements from real LEO satellites. The generalized noise model that was calculated is applied here to simulate measurement error. It is also assumed that the receiver has a knowledge of these noise statistics so that they can be utilized in estimation.

5.1.2 IEKF Setup

The states are estimated with an IEKF as introduced in Section 3.5.1. The IEKF optimizes a nonlinear function for the measurement update, and the solution to this nonlinear function is

applied as a measurement with the Kalman Filter equations. To initialize the filter, Equations (5.1-5.2) show the initial state estimate and covariance passed to the Kalman Filter.

$$\hat{x}_0 = \begin{bmatrix} \delta t_u \\ \dot{\delta} t_u \end{bmatrix} \tag{5.1}$$

$$P_0 = \begin{bmatrix} 5e^{-6} & 0 \\ 0 & 1e^{-8} \end{bmatrix} \tag{5.2}$$

The state vector is initialized to the true bias and drift, and the initial uncertainty is initialized to 5 microseconds for the bias and 10 nanoseconds per second for the drift.

5.1.3 Monte Carlo Scenarios

In order to evaluate the true statistics of the proposed solution, a set of scenarios were tested using a Monte Carlo (MC) approach. The MC simulations produced a mean error and associated covariance which can be directly compared to the mean and covariance of the filter. This will ensure that the filter is correctly reporting its error statistics.

Table 5.1 shows the 20 configurations that were tested in MC simulations. The scenarios cover antenna baseline distances from 3 to 20 meters. Clock grades from inexpensive low quality TCXOs up to expensive rubidium atomic standards are tested with these baselines. These tests will describe the quality of hardware and footprint of receiver that would theoretically be required to realize the system.

Table 5.1: Testing Matrix for 20 Simulation Configurations

Baseline Length (m)	3	5	10	15	20
Low Quality TCXO	1	5	9	13	17
High Quality TCXO	2	6	10	14	18
OCXO	3	7	11	15	19
Rubidium	4	8	12	16	20

Each MC test consisted of 50 runs of the filter, and each run was 1000 seconds long. Starlink satellites positions were simulated as a 'proxy constellation'. This means that their positions were used as the positions of the LEO SOPs in the simulation, but the actual Starlink

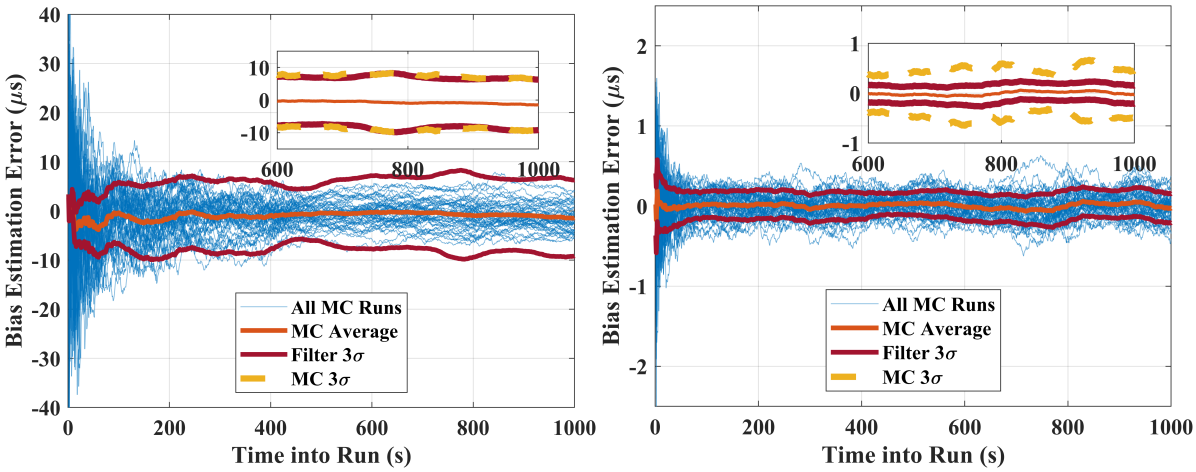

(a) 3 Meter Baseline, Low Quality TCXO

(b) 20 Meter Baseline, Low Quality TCXO

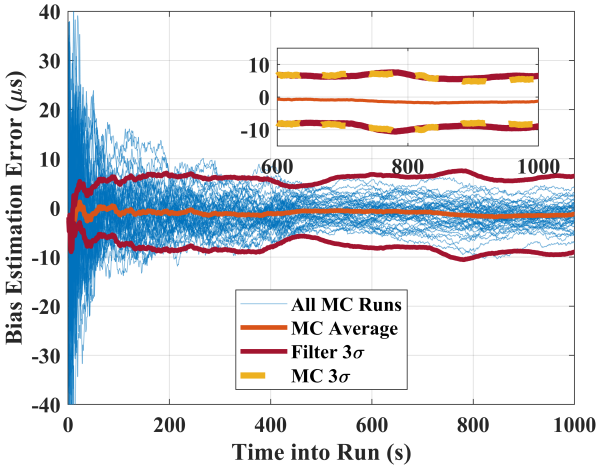

(c) 3 Meter Baseline, High Quality TCXO

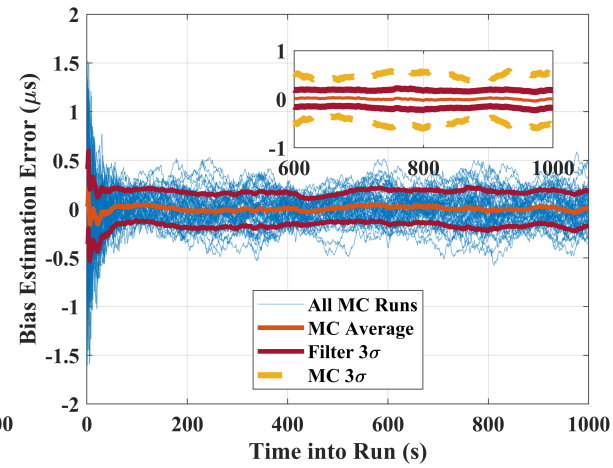

(d) 20 Meter Baseline, High Quality TCXO

Figure 5.2: Receiver Performance with Low and High Quality TCXOs

signal structure was not used. Starlink was chosen because of the large number of satellites in orbit, guaranteeing good geometric diversity at all times.

5.2 Simulation Results

This section details the results of the MC simulations used to verify the system under test. Error plots are shown confirming system performance. System accuracy is analyzed to ascertain whether or not the system can meet the 1μs benchmark of timing performance.

5.2.1 Timing Error Results

Figure 5.2 shows initial results from four of the test scenarios listed in Table 5.1. These correspond to the low and high quality TCXOs at baseline lengths of 3 and 20 meters, effectively

showing a best and worst case for these cheaper clocks. The blue lines in the plots show all 50 MC runs overlaid, showing filter performance for randomized noise. The orange line running down the center is the error mean, and the maroon lines show the IEKF's reported 3σ (>99%) accuracy. The inset figure in the top right shows the last 400 seconds of the run, with blue lines removed for clarity. The inset figure shows how the error dynamics of the filter look at steady state operation. Additionally, these inset figures have the MC 3σ plotted in yellow for comparison to the filter's reported accuracy.

The results show that there is little performance difference between the two variants of TCXO clocks. When the baseline between antennas is short, both struggle to produce good timing estimates. By the end of the run, they have reached an accuracy of around 10 microseconds. With 20 meter baselines, however, the accuracy improves to under 1 microsecond, the target accuracy. The 20 meter baselines show a disagreement between the filter's reported accuracy and the MC calculated accuracy. This disagreement indicates that the Q matrix of the IEKF needs to be tuned upward for these particular receiver implementations. The 20 meter baseline low quality TCXO simulation as well as the 20 meter baseline high quality TCXO simulation were re-run with an inflated Q matrix. The results shown in Figure 5.4 have Monte Carlo covariance and filter reported covariances that match.

Figure 5.3 shows the same type of results as Figure 5.2 but for the two higher grades of clock. The OCXO and Rubidium perform very similarly to the inexpensive clocks for the 3 meter baseline test. This indicates that at short baselines, AoA accuracy arising from baseline length is the constraining factor in receiver accuracy. For long baselines, the OCXO and Rubidium drastically outperform the low and high quality TCXOs. They both have accuracies of around 200 nanoseconds by the end of the simulation. Additionally, there is good agreement between the MC simulation accuracy and the filter accuracy. This indicates that the filter is successfully estimating the mean and covariance of the states.

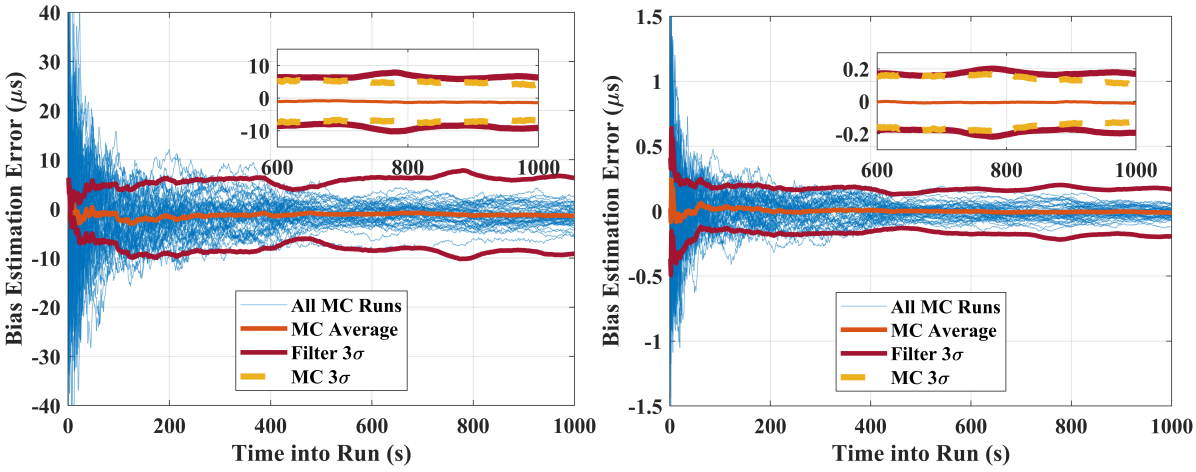

(a) 3 Meter Baseline, OCXO

(b) 20 Meter Baseline, OCXO

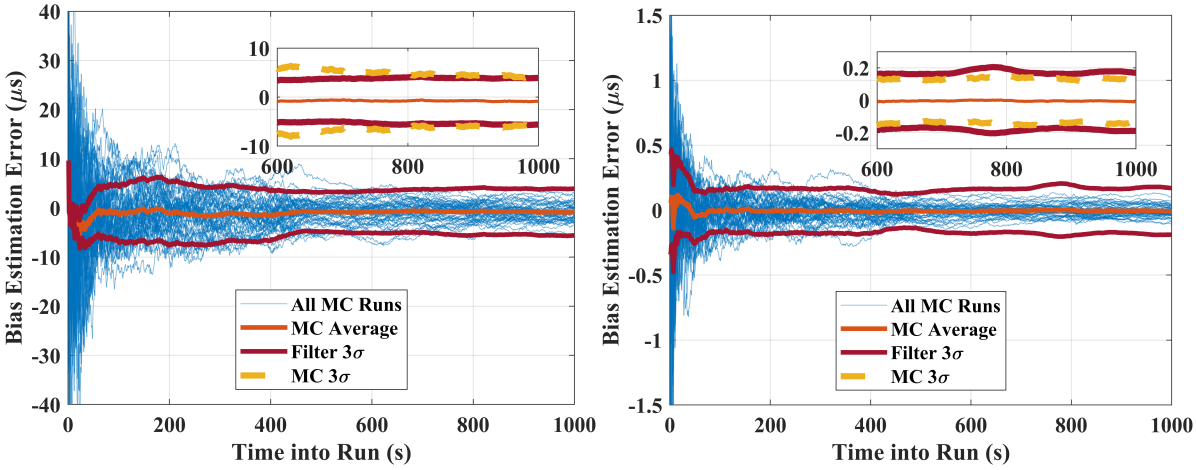

(c) 3 Meter Baseline, Rubidium

(d) 20 Meter Baseline, Rubidium

Figure 5.3: Receiver Performance with OCXO and Rubidium

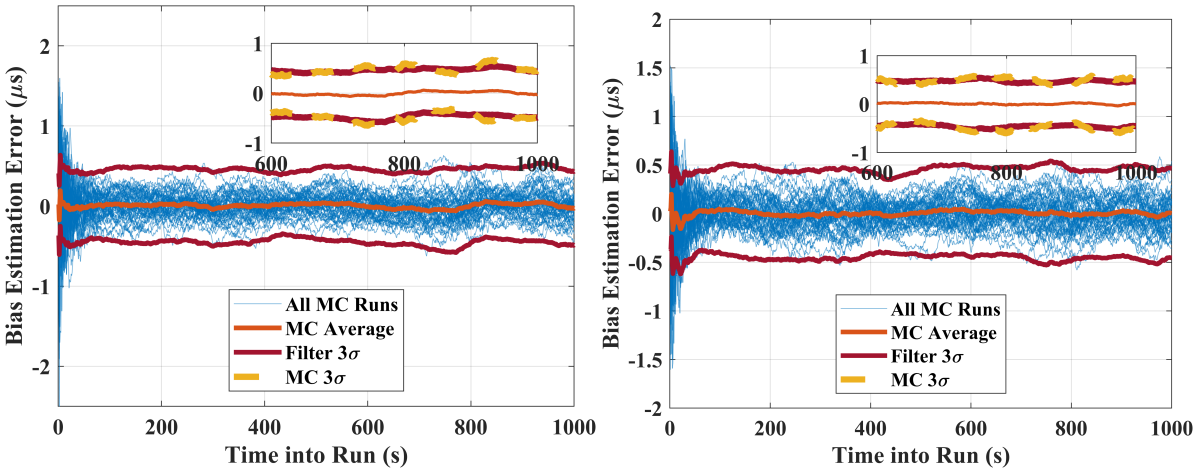

(a) 20 Meter Baseline, Low Quality TCXO

(b) 20 Meter Baseline, High Quality TCXO

Figure 5.4: Timing Simulations with Re-tuned Filter

5.2.2 Timing Accuracy Benchmark

Figure 5.5 shows the timing accuracy of all 20 configurations tested, organized into subplots by type of clock. Each plot shows the filter's reported accuracy in dashed line compared to the MC accuracy with diamonds. Additionally, the target accuracy of 1μs is drawn in solid black on each of the plots to show visually which configurations meet the benchmark.

For the low and high quality TCXOs, only the 15 and 20 meter configurations were sufficient to achieve 1μs accuracy. The 10 meter configuration very nearly met this goal as well. When clock quality is poor, better quality measurements are necessary to estimate timing dynamics. The shorter baselines provide poorer AoA measurements which, when used by the IEKF, are unable to meet the timing requirement. The OCXO and Rubidium results are shown in Figures 5.5d-5.5e. For these clocks, receivers with 10, 15, and 20 meter baselines meet the 3σ goal. For the receiver with 10 meter baselines, it takes around 5 minutes to converge to the point where this accuracy becomes available. For these two clock configurations, the 20 meter baseline provided timing accuracies of around 100 nanoseconds.

The simulations show that to reach the desired timing accuracy, a trade off between clock quality and antenna baseline length occurs. The simulations indicate that the lowest baseline length theoretically possible is 10 meters, but this is only achievable with more accurate (expensive) clocks. If a less expensive oscillator is required, the distances between the receiving antennas must be increased.

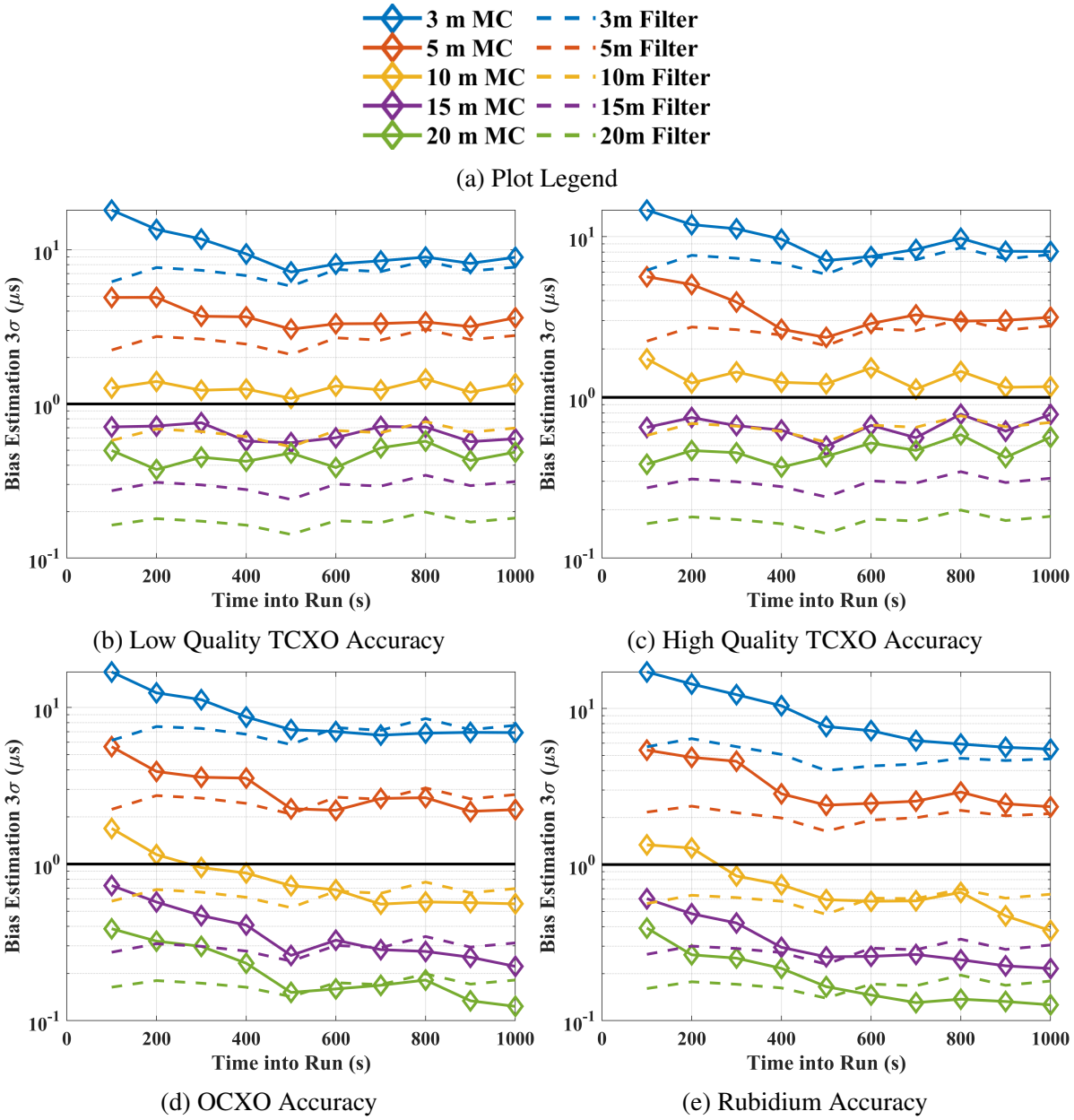

(a) Plot Legend

(b) Low Quality TCXO Accuracy

(c) High Quality TCXO Accuracy

(d) OCXO Accuracy

(e) Rubidium Accuracy

Figure 5.5: Overall Receiver Performance

5.3 Conclusions

In a variety of operating scenarios, the proposed receiver was able to consistently maintain time synchronization to LEO network time, demonstrating successful operation. The Monte Carlo simulations performed tested the receiver's estimation capabilities given a wide variety of antenna baseline distances and receiver oscillator types. For the baseline distances tested, improvement in timing estimates was observed for longer baselines due to the resulting higher quality AoA measurements. For the clock grades simulated, moving from a cheaper TCXO clock to an OCXO or a rubidium clock provided large performance gains due to more certainty in the IEKF. The results showed that for sufficient baseline length and clock quality, meeting the accuracy benchmark of 1 μs was possible using the designed receiver.

Chapter 6

Conclusions and Future Work

This work has provided a design and analysis of a receiver capable of maintaining precise time estimates in the event of a GPS outage. To validate this new solution, a series of Monte Carlo studies was carried out to assess the proposed receiver with a variety of different antenna baseline lengths and clock oscillator types. These simulations carried the benefit of a realistic measurement noise profile provided by a LEO satellite emitter noise analysis. This analysis characterized the noise on LEO navigation measurements using live sky data.

The receiver was able to estimate its clock bias during a simulated GPS outage. The accuracy that the receiver's filter achieved was dependent on the distance between receiving antennas and the type of clock that the receiver used. For baselines of 15 meters and higher, the receiver was able to meet the 1μs timing benchmark with a TCXO clock. When equipped with a more accurate OCXO or Rubidium clock, the receiver was able to meet this requirement for baselines 10 meters and higher.

This work has much room for potential improvement. First, the algorithm includes no dynamic model for the satellites being tracked, they are merely estimated on an epoch-by-epoch basis. An orbital model could refine these positions further, allowing for better timing estimates. Second, the work in experimental noise identification could be expanded to calculate a noise model for the measured AoA. This would allow for a complete end-to-end simulation of the system. Finally, the work would benefit from a real-time implementation of the algorithm for final verification.

Bibliography

[1] Michael J. Dunn. *Directions 2023: Advancing GPS to Meet the Future*. GPS World. Section: Featured Stories. Mar. 6, 2023. URL: https://www.gpsworld.com/directions-2023-advancing-gps-to-meet-the-future/ (visited on 07/01/2024).

[2] United States Department of Defense. *Global Positioning System Standard Positioning Service Performance Standard*. Apr. 15, 2020. URL: https://www.gps.gov/technical/ps/2020-SPS-performance-standard.pdf (visited on 08/13/2024).

[3] David Last. "GNSS: The Present Imperfect". In: *Inside GNSS* (2010).

[4] Jahshan Bhatti and Todd E. Humphreys. "Hostile Control of Ships via False GPS Signals: Demonstration and Detection". In: *NAVIGATION* 64.1 (2017). _eprint: https://onlinelibrary.wiley.c pp. 51–66. ISSN: 2161-4296. DOI: 10.1002/navi.183. URL: https://onlinelibrary.wiley.com/doi/abs/10.1002/navi.183 (visited on 08/15/2024).

[5] Tyler G.R. Reid et al. "Broadband LEO Constellations for Navigation". In: *NAVIGATION* 65.2 (2018). _eprint: https://onlinelibrary.wiley.com/doi/pdf/10.1002/navi.234, pp. 205–220. ISSN: 2161-4296. DOI: 10.1002/navi.234. URL: https://onlinelibrary.wiley.com/doi/abs/10.1002/navi.234 (visited on 07/02/2024).

[6] Nadim Khairallah and Zaher Kassas M. "Ephemeris Closed-Loop Tracking of LEO Satellites with Pseudorange and Doppler Measurements". In: ION GNSS+. St. Louis, MO, 2021.

[7] Ralph Sabbagh and Zaher Kassas M. “Observability Analysis of Receiver Localization via Pseudorange Measurements From a Single LEO Satellite”. In: IEEE Control Systems Letters. Vol. 7. 2023, pp. 571–576.

[8] Kan Wang and Ahmed El-Mowafy. “LEO satellite clock analysis and prediction for positioning applications”. In: *Geo-spatial Information Science* 25.1 (Jan. 2, 2022). Publisher: Taylor & Francis _eprint: https://doi.org/10.1080/10095020.2021.1917310, pp. 14–33. ISSN: 1009-5020. DOI: 10.1080/10095020.2021.1917310. URL: https://doi.org/10.1080/10095020.2021.1917310 (visited on 10/23/2024).

[9] Florian Kunzi and Oliver Montenbruck. “Precise Onboard Time Synchronization for LEO Satellites”. In: *NAVIGATION: Journal of the Institute of Navigation* 69.3 (Sept. 21, 2022). Publisher: Institute of Navigation Section: Original Article. ISSN: 0028-1522, 2161-4296. DOI: 10.33012/navi.531. URL: https://navi.ion.org/content/69/3/navi.531 (visited on 07/01/2024).

[10] R. Wang, J. Liu, and Q. M. Zhang. “Propagation errors analysis of TLE data”. In: *Advances in Space Research* 43.7 (Apr. 1, 2009), pp. 1065–1069. ISSN: 0273-1177. DOI: 10.1016/j.asr.2008.11.017. URL: https://www.sciencedirect.com/science/article/pii/S0273117708006121 (visited on 07/02/2024).

[11] Sterling Thompson, Scott Martin, and David Bevly. “Single Differenced Doppler Positioning with Low Earth Orbit Signals of Opportunity and Angle of Arrival Estimation”. In: 2021 International Technical Meeting of The Institute of Navigation. Online, Feb. 23, 2021, pp. 497–509. DOI: 10.33012/2021.17845. URL: https://www.ion.org/publications/abstract.cfm?articleID=17845 (visited on 08/27/2024).

[12] Kenneth A Fisher and John F Raquet. “Precision Position, Navigation, and Timing without the Global Positioning System”. In: ().

[13] *Xona Broadcasts Demo PNT Signals From Low Earth Orbit*. Xona Space Systems. URL: https://www.xonaspace.com/xonademospntsignals (visited on 12/10/2024).

[14] Debra Werner. *TrustPoint wins SpaceWERX contracts for alternative PNT*. SpaceNews. Aug. 21, 2024. URL: https://spacenews.com/trustpoint-wins-spacewerx-contracts-for-alternative-pnt/ (visited on 12/10/2024).

[15] D. Orgiazzi, P. Tavella, and F. Lahaye. "Experimental assessment of the time transfer capability of precise point positioning (PPP)". In: *Proceedings of the 2005 IEEE International Frequency Control Symposium and Exposition, 2005.* Proceedings of the 2005 IEEE International Frequency Control Symposium and Exposition, 2005. ISSN: 2327-1949. Aug. 2005, pp. 337–345. DOI: 10.1109/FREQ.2005.1573955. URL: https://ieeexplore.ieee.org/abstract/document/1573955/authors#authors (visited on 07/01/2024).

[16] Denis Laurichesse et al. "Integer Ambiguity Resolution on Undifferenced GPS Phase Measurements and Its Application to PPP and Satellite Precise Orbit Determination". In: *NAVIGATION* 56.2 (2009). _eprint: https://onlinelibrary.wiley.com/doi/pdf/10.1002/j.2161-4296.2009.tb01750.x, pp. 135–149. ISSN: 2161-4296. DOI: 10.1002/j.2161-4296.2009.tb01750.x. URL: https://onlinelibrary.wiley.com/doi/abs/10.1002/j.2161-4296.2009.tb01750.x (visited on 04/24/2024).

[17] Jianghui Geng et al. "Integer ambiguity resolution in precise point positioning: method comparison". In: *Journal of Geodesy* 84.9 (Sept. 1, 2010), pp. 569–581. ISSN: 1432-1394. DOI: 10.1007/s00190-010-0399-x. URL: https://doi.org/10.1007/s00190-010-0399-x (visited on 04/23/2024).

[18] Mingyue Liu et al. "Study of Fast and Reliable Time Transfer Methods Using Low Earth Orbit Enhancement". In: *Remote Sensing* 16.11 (Jan. 2024). Number: 11 Publisher: Multidisciplinary Digital Publishing Institute, p. 2044. ISSN: 2072-4292. DOI: 10.3390/rs16112044. URL: https://www.mdpi.com/2072-4292/16/11/2044 (visited on 07/01/2024).

[19] Xingxing Li et al. "LEO constellation-augmented multi-GNSS for rapid PPP convergence". In: *Journal of Geodesy* 93.5 (May 1, 2019), pp. 749–764. ISSN: 1432-1394.

DOI: 10.1007/s00190-018-1195-2. URL: https://doi.org/10.1007/s00190-018-1195-2 (visited on 07/02/2024).

[20] Austin Smith. "Timing Evaluation of Iridium Satellite Time and Location Signal: Measurement-Level Implementation and Receiver Hardware Time Interval Comparison". PhD thesis. Auburn University, 2023.

[21] Peter Johnson B, Andrew Novick N, and Michael Lombardi A. "Measuring the Timing Accuracy of Satellite Time and Location (STL) Receivers". In: ION PTTI. Long Beach, CA: Institiute of Navigation, 2023.

[22] Inside GNSS. *Test Confirms Timing Resilience of LEO Time Service Underground, Indoors - Inside GNSS - Global Navigation Satellite Systems Engineering, Policy, and Design*. URL: https://insidegnss.com/test-confirms-timing-resilience-of-leo-time-service-underground-indoors/ (visited on 07/01/2024).

[23] Landon Boyd and David M. Bevly. "Meeting Modern Timing Demands with LEO Satellite Signals and Long Baseline Phase Interferometry". In: ION 2024 Pacific PNT Meeting. Honolulu, Hawaii, May 8, 2024, pp. 293–304. DOI: 10.33012/2024.19610. URL: https://www.ion.org/publications/abstract.cfm?articleID=19610 (visited on 08/27/2024).

[24] NIST. *A Walk Through Time - World Time Scales — NIST*. URL: https://www.nist.gov/pml/time-and-frequency-division/popular-links/walk-through-time/walk-through-time-world-time-scales (visited on 07/02/2024).

[25] Stephen B. Weinstein. "The history of orthogonal frequency-division multiplexing [History of Communications]". In: *IEEE Communications Magazine* 47.11 (Nov. 2009). Conference Name: IEEE Communications Magazine, pp. 26–35. ISSN: 1558-1896. DOI: 10.1109/MCOM.2009.5307460. URL: https://ieeexplore.ieee.org/document/5307460 (visited on 07/02/2024).

[26] ADTRAN. *Why time-sync is so important to the smart power grid*. 2019. URL: https://www.blog.adtran.com/en/why-time-sync-is-so-important-to-the-smart-power-grid (visited on 07/02/2024).

[27] United States Naval Observatory. *USNO GPS Time Transfer*. URL: https://www.cnmoc.usff.navy.mil/Our-Commands/United-States-Naval-Observatory/Precise-Time-Department/Global-Positioning-System/USNO-GPS-Time-Transfer/ (visited on 07/02/2024).

[28] United States Naval Observatory. *The USNO Master Clock*. URL: https://www.cnmoc.usff.navy.mil/Our-Commands/United-States-Naval-Observatory/Precise-Time-Department/The-USNO-Master-Clock/The-USNO-Master-Clock/ (visited on 07/02/2024).

[29] BIPM. *Time metrology - BIPM*. URL: https://www.bipm.org/en/time-metrology (visited on 08/13/2024).

[30] NIST. *NIST Time Frequently Asked Questions (FAQ) — NIST*. URL: https://www.nist.gov/pml/time-and-frequency-division/nist-time-frequently-asked-questions-faq#utcnist (visited on 08/13/2024).

[31] NIST. *Introduction to UTC(NIST) — NIST*. URL: https://www.nist.gov/pml/time-and-frequency-division/time-realization/utcnist-time-scale-0/introduction-utcnist (visited on 08/13/2024).

[32] Edward Powers. "Implementing Galileo/GNSS to GPS Time Offset". URL: https://www.gps.gov/governance/advisory/meetings/2013-05/powers.pdf (visited on 08/13/2024).

[33] United States Space Systems Command. *GPS Interface Control Document*. Aug. 2022. URL: https://www.gps.gov/technical/icwg/IS-GPS-200N.pdf (visited on 08/13/2024).

[34] Pratap Misra and Per K. Enge. *Global Positioning System: Signals, Measurements, and Performance*. 2nd ed. Ganga Jamuna Press, 2012.

[35] Elliott D. Kaplan and Christopher J. Hegarty. *Understanding GPS/GNSS Principles and Applications*. 3rd ed. Artech House, 2017.

[36] Michael A. Lombardi. "Microsecond accuracy at multiple sites: is it possible without GPS?" In: *IEEE Instrumentation & Measurement Magazine* 15.5 (Oct. 2012). Conference Name: IEEE Instrumentation & Measurement Magazine, pp. 14–21. ISSN: 1941-0123. DOI: 10.1109/MIM.2012.6314510. URL: https://ieeexplore.ieee.org/abstract/document/6314510 (visited on 07/04/2024).

[37] Nicolas Guyennon et al. "Further Characterization of the Time Transfer Capabilities of Precise Point Positioning (PPP)". In: *2007 IEEE International Frequency Control Symposium Joint with the 21st European Frequency and Time Forum*. 2007 IEEE International Frequency Control Symposium Joint with the 21st European Frequency and Time Forum. ISSN: 2327-1949. May 2007, pp. 399–404. DOI: 10.1109/FREQ.2007.4319105. URL: https://ieeexplore.ieee.org/abstract/document/4319105 (visited on 08/15/2024).

[38] Andrey Soloviev and Frank van Graas. "Utilizing multipath reflections in deeply integrated GPS/INS architecture for navigation in urban environments". In: *2008 IEEE/ION Position, Location and Navigation Symposium*. 2008 IEEE/ION Position, Location and Navigation Symposium. ISSN: 2153-3598. May 2008, pp. 383–393. DOI: 10.1109/PLANS.2008.4570094. URL: https://ieeexplore.ieee.org/abstract/document/4570094 (visited on 07/03/2024).

[39] CISA. *Global Positioning System (GPS) Interference Event - Denver, CO*. Dec. 2022.

[40] Inside GNSS. *The Unsolved Mystery of the 2022 Texas Interference - Inside GNSS - Global Navigation Satellite Systems Engineering, Policy, and Design*. URL: https://insidegnss.com/the-unsolved-mystery-of-the-2022-texas-interference/ (visited on 07/03/2024).

[41] *GPS Jamming Map*. In collab. with John Wiseman. July 2022. URL: https://gpsjam.org/.

[42] Mark L. Psiaki and Todd E. Humphreys. “GNSS Spoofing and Detection”. In: *Proceedings of the IEEE* 104.6 (June 2016). Conference Name: Proceedings of the IEEE, pp. 1258–1270. ISSN: 1558-2256. DOI: 10.1109/JPROC.2016.2526658. URL: https://ieeexplore.ieee.org/abstract/document/7445815 (visited on 08/15/2024).

[43] Benjamin J. Clark. “GPS/INS Operation in Shadowed Environments”. PhD thesis. Auburn University, 2008. URL: https://etd.auburn.edu/handle/10415/1223.

[44] Janis Balodis, Madara Normand, and Inese Varna. “Extreme Solar Events’ Impact on GPS Positioning Results”. In: *Remote Sensing* 13.18 (Jan. 2021). Number: 18 Publisher: Multidisciplinary Digital Publishing Institute, p. 3624. ISSN: 2072-4292. DOI: 10.3390/rs13183624. URL: https://www.mdpi.com/2072-4292/13/18/3624 (visited on 07/03/2024).

[45] Patricia H. Doherty et al. “Ionospheric Scintillation Effects on GPS in the Equatorial and Auroral Regions”. In: *NAVIGATION* 50.4 (2003). _eprint: https://onlinelibrary.wiley.com/doi/pdf/10.100 4296.2003.tb00332.x, pp. 235–245. ISSN: 2161-4296. DOI: 10.1002/j.2161-4296.2003.tb00332.x. URL: https://onlinelibrary.wiley.com/doi/abs/10.1002/j.2161-4296.2003.tb00332.x (visited on 07/03/2024).

[46] T. S. Kelso. *Celestrak*. URL: https://celestrak.org/.

[47] Zaher M. Kassas, Nadim Khairallah, and Sharbel Kozhaya. “Ad Astra: Simultaneous Tracking and Navigation With Megaconstellation LEO Satellites”. In: *IEEE Aerospace and Electronic Systems Magazine* (2024). Conference Name: IEEE Aerospace and Electronic Systems Magazine, pp. 1–19. ISSN: 1557-959X. DOI: 10.1109/MAES.2023.3267440. URL: https://ieeexplore.ieee.org/abstract/document/10388052 (visited on 08/15/2024).

[48] Trier Mortlock and Zaher M. Kassas. “Assessing Machine Learning for LEO Satellite Orbit Determination in Simultaneous Tracking and Navigation”. In: *2021 IEEE Aerospace Conference (50100)*. 2021 IEEE Aerospace Conference (50100). ISSN: 1095-323X. Mar. 2021, pp. 1–8. DOI: 10.1109/AERO50100.2021.9438144. URL:

https://ieeexplore.ieee.org/abstract/document/9438144 (visited on 08/15/2024).

[49] Pei Chen, Jian Zhang, and Xiucong Sun. "Real-time kinematic positioning of LEO satellites using a single-frequency GPS receiver". In: *GPS Solutions* 21.3 (July 1, 2017), pp. 973–984. ISSN: 1521-1886. DOI: 10.1007/s10291-016-0586-1. URL: https://doi.org/10.1007/s10291-016-0586-1 (visited on 07/03/2024).

[50] Zhixin Yang et al. "Real-Time Estimation of Low Earth Orbit (LEO) Satellite Clock Based on Ground Tracking Stations". In: *Remote Sensing* 12.12 (Jan. 2020). Number: 12 Publisher: Multidisciplinary Digital Publishing Institute, p. 2050. ISSN: 2072-4292. DOI: 10.3390/rs12122050. URL: https://www.mdpi.com/2072-4292/12/12/2050 (visited on 07/01/2024).

[51] Guigen Nie et al. "Research on LEO Satellites Time Synchronization with GPS Receivers Onboard". In: *2007 IEEE International Frequency Control Symposium Joint with the 21st European Frequency and Time Forum*. 2007 IEEE International Frequency Control Symposium Joint with the 21st European Frequency and Time Forum. ISSN: 2327-1949. May 2007, pp. 896–900. DOI: 10.1109/FREQ.2007.4319208. URL: https://ieeexplore.ieee.org/document/4319208 (visited on 07/03/2024).

[52] John A. Pratt. "New Time and Multipath Augmentations for the Global Positioning System". ISBN: 9781339363837. PhD thesis. United States – Colorado: University of Colorado at Boulder. 182 pp. URL: https://www.proquest.com/docview/1755696649/abstract/3C90D243EB17494DPQ/1 (visited on 08/15/2024).

[53] John Pratt et al. "Satellite clock bias estimation for iGPS". In: *GPS Solutions* 17.3 (July 1, 2013), pp. 381–389. ISSN: 1521-1886. DOI: 10.1007/s10291-012-0286-4. URL: https://doi.org/10.1007/s10291-012-0286-4 (visited on 08/06/2024).

[54] Todd E. Humphreys et al. “Signal Structure of the Starlink Ku-Band Downlink”. In: *IEEE Transactions on Aerospace and Electronic Systems* (2023), pp. 1–16. ISSN: 0018-9251, 1557-9603, 2371-9877. DOI: 10.1109/TAES.2023.3268610. URL: https://ieeexplore.ieee.org/document/10107477/ (visited on 08/16/2024).

[55] ICAO. *ICAO Technical Manual For Iridium Aeronautical Mobile Satellite (Route) Service*. May 19, 2006. URL: https://www.icao.int/safety/acp/ACPWGF/ACP-WG-M-11/ACP-WGM11-WP04-Draft%20Iridium%20Technical%20Specification%20Version%201.1%20-%20051906.pdf (visited on 07/20/2024).

[56] Nadim Khairallah and Zaher M. Kassas. “An Interacting Multiple Model Estimator of LEO Satellite Clocks for Improved Positioning”. In: *2022 IEEE 95th Vehicular Technology Conference: (VTC2022-Spring)*. 2022 IEEE 95th Vehicular Technology Conference (VTC2022-Spring). Helsinki, Finland: IEEE, June 2022, pp. 1–5. ISBN: 978-1-66548-243-1. DOI: 10.1109/VTC2022-Spring54318.2022.9860828. URL: https://ieeexplore.ieee.org/document/9860828/ (visited on 07/05/2024).

[57] Quan Huang, Shaopeng Wei, and Lei Zhang. “Radar Interferometric Phase Ambiguity Resolution Using Viterbi Algorithm for High-Precision Space Target Positioning”. In: *IEEE Signal Processing Letters* 30 (2023). Conference Name: IEEE Signal Processing Letters, pp. 1242–1246. ISSN: 1558-2361. DOI: 10.1109/LSP.2023.3313092. URL: https://ieeexplore.ieee.org/document/10244102 (visited on 07/05/2024).

[58] Peter Ly. “Fast and Unambiguous Direction Finding for Digital Radar Intercept Receivers”. PhD thesis. Adelaide, South Australia: University of Adelaide, 2013. URL: https://digital.library.adelaide.edu.au/dspace/bitstream/2440/90332/4/02whole.pdf.

[59] Mohd Noor Islam et al. “Doppler and Angle of Arrival Estimation from Digitally Modulated Satellite Signals in Passive RF Space Domain Awareness”. In: (2021).

[60] Antonello Florio et al. “LEO-Based Coarse Positioning Through Angle-of-Arrival Estimation of Signals of Opportunity”. In: *IEEE Access* 12 (2024). Conference Name: IEEE Access, pp. 17446–17459. ISSN: 2169-3536. DOI: 10.1109/ACCESS.2024.3359440. URL: https://ieeexplore.ieee.org/document/10415436/?arnumber=10415436 (visited on 12/11/2024).

[61] Mark L. Psiaki. “Navigation using carrier Doppler shift from a LEO constellation: TRANSIT on steroids”. In: *NAVIGATION* 68.3 (2021). _eprint: https://onlinelibrary.wiley.com/doi/pdf/10.1002 pp. 621–641. ISSN: 2161-4296. DOI: 10.1002/navi.438. URL: https://onlinelibrary.wiley.com/doi/abs/10.1002/navi.438 (visited on 08/23/2024).

[62] Jindřich Havlík and Ondřej Straka. “Performance evaluation of iterated extended Kalman filter with variable step-length”. In: *Journal of Physics: Conference Series* 659 (Nov. 19, 2015), p. 012022. ISSN: 1742-6588, 1742-6596. DOI: 10.1088/1742-6596/659/1/012022. URL: https://iopscience.iop.org/article/10.1088/1742-6596/659/1/012022 (visited on 08/22/2024).

[63] *navsim*. URL: https://github.com/navsquad/navsim.

[64] Iridium. *Network: Iridium Satellite Communications*. URL: https://www.iridium.com/network/.

[65] Tereza Pultarova et al. “Starlink satellites: Facts, tracking and impact on astronomy”. In: *Space.com* (July 1, 2024). URL: https://www.space.com/spacex-starlink-satellites.html.

[66] UT Austin. *AstriaGraph*. URL: http://astria.tacc.utexas.edu/AstriaGraph/ (visited on 08/16/2024).

[67] Felix R. Hoots and Ronald L. Roehrich. *Models for Propagation of NORAD Element Sets:* Fort Belvoir, VA: Defense Technical Information Center, Dec. 1, 1980. DOI: 10.21236/ADA093554. URL: http://www.dtic.mil/docs/citations/ADA093554 (visited on 08/16/2024).

[68] Lorenzo Galleani. “A tutorial on the two-state model of the atomic clock noise”. In: *Metrologia* 45.6 (Dec. 2008), S175. ISSN: 0026-1394. DOI: 10.1088/0026-1394/45/6/S23. URL: https://dx.doi.org/10.1088/0026-1394/45/6/S23 (visited on 07/08/2024).

[69] D.W. Allan. “Statistics of atomic frequency standards”. In: *Proceedings of the IEEE* 54.2 (1966), pp. 221–230. ISSN: 0018-9219. DOI: 10.1109/PROC.1966.4634. URL: http://ieeexplore.ieee.org/document/1446564/ (visited on 07/08/2024).

[70] C. Zucca and P. Tavella. “The clock model and its relationship with the Allan and related variances”. In: *IEEE Transactions on Ultrasonics, Ferroelectrics, and Frequency Control* 52.2 (Feb. 2005). Conference Name: IEEE Transactions on Ultrasonics, Ferroelectrics, and Frequency Control, pp. 289–296. ISSN: 1525-8955. DOI: 10.1109/TUFFC.2005.1406554. URL: https://ieeexplore.ieee.org/abstract/document/1406554 (visited on 07/08/2024).

[71] R. G. Brown and P. Y. Huang. *Introduction to random signals and applied Kalman filtering: with MATLAB excercies*. Hoboken, N.J.: Wiley, 2012.

[72] Stanford Research Systems. *PRS10 Rubidium Frequency Standard*. URL: https://www.thinksrs.com/downloads/pdfs/catalog/PRS10c.pdf (visited on 08/09/2024).

[73] Van-Sang Doan et al. “Phase-difference measurement-based angle of arrival estimation using long-baseline interferometer”. In: *IET Radar, Sonar & Navigation* 17.3 (2023). _eprint: https://onlinelibrary.wiley.com/doi/pdf/10.1049/rsn2.12352, pp. 449–465. ISSN: 1751-8792. DOI: 10.1049/rsn2.12352. URL: https://onlinelibrary.wiley.com/doi/abs/10.1049/rsn2.12352 (visited on 08/23/2024).

[74] Joshua J. Morales et al. “Orbit Modeling for Simultaneous Tracking and Navigation using LEO Satellite Signals”. In: 32nd International Technical Meeting of the Satellite Division of The Institute of Navigation (ION GNSS+ 2019). Miami, Florida, Oct. 11, 2019, pp. 2090–2099. DOI: 10.33012/2019.17029. URL: https://www.

ion.org/publications/abstract.cfm?articleID=17029 (visited on 11/21/2024).

Appendix A

AoA Estimation From TLE-Level Satellite Position Data

This appendix details a possible solution for resolving ambiguous AoAs using publicly available TLE data. Since the receiver designed in this thesis relies on AoA measurements, a method is required for obtaining unambiguous differenced phase at two antennas. This method consists of calculating satellite positions from TLE data, and using them along with the known receiver location to calculate a theoretical AoA. This theoretical AoA informs the receiver how many phase cycle wraps have occurred across the antenna baseline, allowing for an accurate measurement of true AoA.

A.1 AoA Ambiguity

Figure A.1 shows the diagram of the differenced carrier phase measurement that is used to construct the AoA. As Section 2.1.4 explained, the carrier phase measurement obtained has

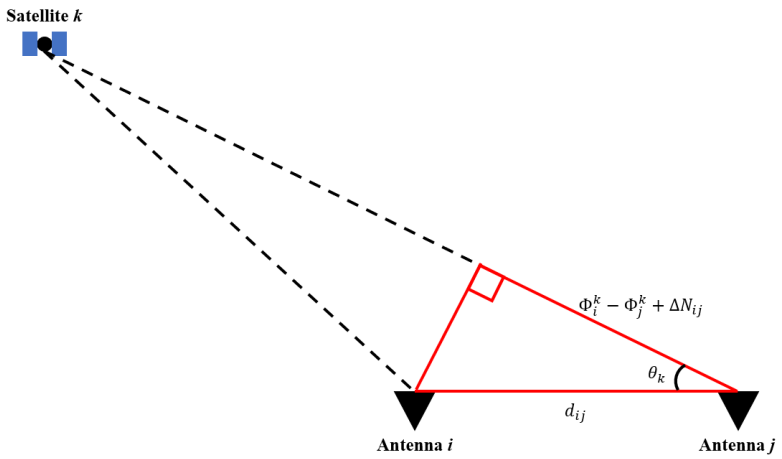

Figure A.1: Differenced Carrier Phase Measurement Diagram

an ambiguous number of integer cycles in the measurement. This number is unknown, and represents the number of carrier cycles in between the emitter and receiver. When carrier phase is differenced as it is in Figure A.1, the differenced measurement contains the difference between the two unknown integers ΔN_{ij}.

ΔN_{ij} represents the number of additional carrier cycles that occur in between antennas i and j. This number cannot be obtained via tracking since tracking hardware can only detect carrier phases in between 0 and 2π. As an example, suppose a carrier has a wavelength of 1 meter and that this carrier must travel 3.5 extra meters to reach antenna j in Figure A.1. The amount of unambiguous phase between the two antennas is given in Equation A.1.

$$\Delta\Phi_{ij}^{k} = (3.5 - 1) * 2\pi = 5\pi \text{ [rad]} \tag{A.1}$$

For this example, there are 5π radians of carrier distance between the two antennas. The tracking hardware, however, can only detect phase differences between 0 and 2π. This means the measured differenced phase will actually be:

$$\Delta\tilde{\Phi}_{ij}^{k} = mod(5\pi, 2\pi) = [5\pi]_{2\pi} = 0.5 \text{ [cycles]} \tag{A.2}$$

Even though the carrier has rotated 810 degrees between the antennas, the receiver will read a differenced phase of 180 degrees. In order to recover the true differenced carrier, and therefore the AoA, the number of wrapped cycles must be estimated from another data source. Each whole cycle that is possible between the two antennas gives rise to a different AoA, with only one AoA representing the true measurement. The total number (N) of ambiguities that can occur in an antenna system is a function of carrier wavelength and baseline distance, and is given in Equation A.3.

$$N = \text{round}\left[\frac{2d}{\lambda}\right] \tag{A.3}$$

For this analysis, a nominal carrier frequency of 1626 MHz is assumed, being the in Iridium's portion of the L Band. This frequency gives a carrier wavelength of 18.4 cm. In the thesis,

Table A.1: Possible AoAs for each Baseline Tested

Baseline [m]	3	5	10	15	20
N	33	54	108	163	217

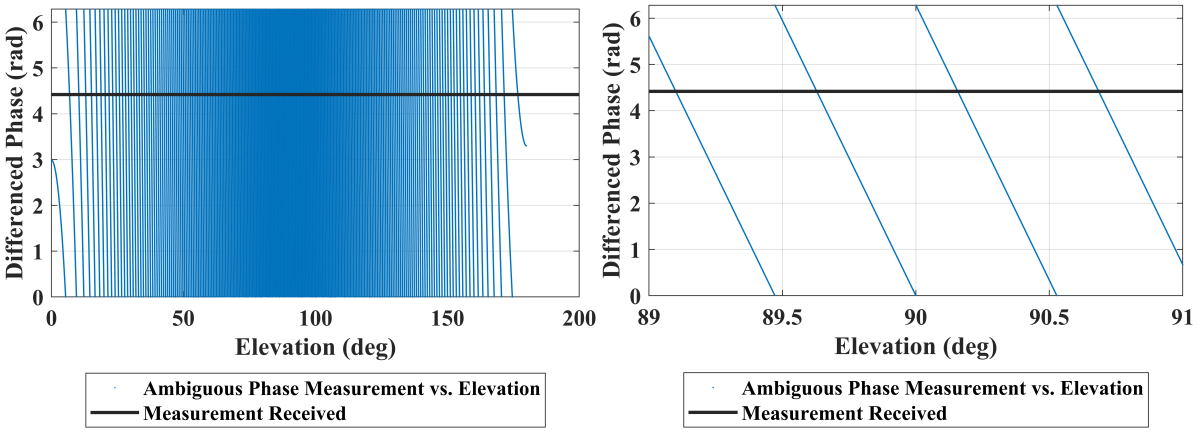

(a) Integer Search Space for 20 Meter Spacing

(b) Closeup

Figure A.2: Integer Search Space

baselines of 3, 5, 10, 15, and 20 meters were tested. Table A.1 shows the number of possible AoAs that arise for each of the receiver configurations tested in this thesis.

The longer baseline receiver configurations give higher quality AoAs, but the trade off is that estimating this AoA is more difficult due to the larger search space of N. This search space is shown graphically in Figure A.2. Figure A.2a on the left shows all possible differenced carrier phase measurements as a function of the true elevation angle of the AoA. The black line indicates the measured AoA. Anywhere the black line touches the discontinuous blue line is a potential AoA. According to Table A.1, there are 217 such intersections. Figure A.2b on the right shows an expanded view centered at zenith where the lines are most dense. In order to know which of these intersections is the true AoA then, the AoA must be known to within half a degree. This level of knowledge would constrain the measurement to one of these lines, allowing the receiver to use the precise differenced phase knowledge to get an even higher fidelity AoA.

In order to constrain the AoA to this half degree requirement, TLE-accurate satellite positions and geometry can be used. The next section proves that TLE knowledge is sufficient to meet this requirement.

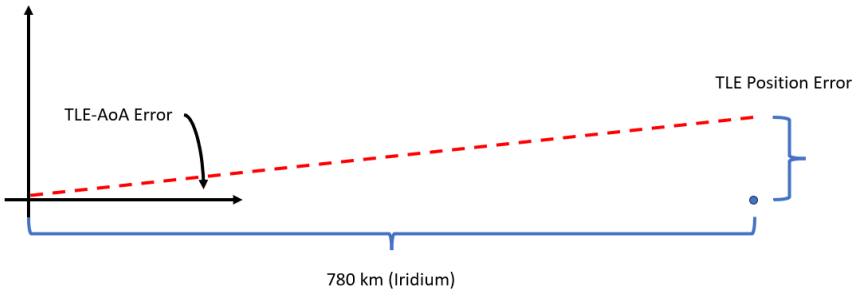

Figure A.3: TLE Position Error Projected onto AoA Error

A.2 TLE-AoA Calculation

To determine if TLE-level data is sufficient to provide half degree angular resolution, it must be shown that TLE errors do not move the change the geometrical angle of arrival by more than half a degree. To accomplish this, the angle of a arrival of a far away point was calculated for varying levels of error. To develop a worst-case envelope, the entirety of the TLE position error is projected tangent to the true radial direction. Figure A.3 shows the testing setup.

The Iridium satellites orbit at 780 km. For this orbital altitude, it was found that a TLE position error of 6.807 km was necessary to introduce one half degree of angular error. This means that if the TLE used has less that 6.8 km of position error, it will be enough to estimate AoA unambiguously. This is the case, as the expected value for LEO TLE error is on the order of 1-5 km [74]. This means that AoA estimation is feasible for all of the baselines tested in Chapter 5 of this thesis.